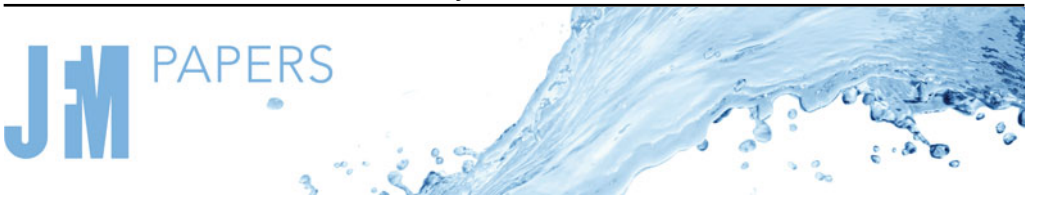
J. Fluid Mech. (2026), *vol.* 1032, A4, doi:10.1017/jfm.2026.11311



Longitudinal stripe formation in bidisperse granular free-surface flows with secondary vortices

Amber P. Pearse[1], **Chris G. Johnson**[1] **and J.M.N.T. Gray**[1]

[1]Department of Mathematics and Manchester Centre for Nonlinear Dynamics, University of Manchester, Oxford Road, Manchester M13 9PL, UK

Corresponding author: J.M.N.T. Gray, nico.gray@manchester.ac.uk

(Received 20 October 2025; revised 5 February 2026; accepted 6 February 2026)

Rapid granular free-surface flows on inclined planes can develop secondary vortices aligned with the dominant flow direction. The reason for their formation remains a subject of research, but plausible mechanisms include instabilities driven by (i) dilatation/compressibility, (ii) normal stress differences and (iii) a self-induced Raleigh–Taylor instability caused by segregation of large–dense and small–light particles. In this paper, a set of novel experiments are performed with large and small particles (of the same bulk density), which form longitudinal stripes due to a combination of secondary recirculation and particle-size segregation. A conceptual model is formulated, in which large particles concentrate in the downwelling sections, small particles concentrate in the upwelling sections and a breaking-size-segregation wave separates the two pure phases from one another. In each secondary vortex, the breaking waves allow the large and small particles to continuously recirculate. Assuming that a series of counter-rotating vortices exist, it is shown that this internal cross-slope structure emerges naturally from solving the gravity-shear-driven segregation-advection equations. When viewed from above, this generates a series of alternating bands of large and small particles, that are sharply separated from one another and are aligned with the downslope direction. Each complete stripe (measured from centre to centre of each large band) is formed by two counter-rotating secondary vortices. Despite the apparent order of the steady-state stripes, it is shown that the individual large and small particle paths form complex interpenetrating co-rotating sub-vortices as they avalanche downslope.

Key words: avalanches, dry granular material, pattern formation

© The Author(s), 2026. Published by Cambridge University Press. This is an Open Access article, distributed under the terms of the Creative Commons Attribution licence (https://creativecommons.org/licenses/by/4.0/), which permits unrestricted re-use, distribution and reproduction, provided the original article is properly cited.

https://doi.org/10.1017/jfm.2026.11311 Published online by Cambridge University Press

1. Introduction

Secondary vortices and other coherent structures are important because they give insights into the rheology of granular flows, which is still a highly active and challenging area of research (Jop, Forterre & Pouliquen 2006; McElwaine, Takagi & Huppert 2012; Barker *et al.* 2015; Heyman *et al.* 2017*b*; Goddard & Lee 2018; Schaeffer *et al.* 2019; Dsouza & Nott 2020; Srivastava *et al.* 2021; Barker *et al.* 2021; Kim & Kamrin 2023). They may also explain the formation of transverse ridges and flow bands, which are frequently observed in long run-out landslides on Earth (Shreve 1966; Post 1967; McSaveney 1978; Dufresne & Davies 2009) and other planetary bodies (Magnarini *et al.* 2019; Magarini *et al.* 2021; Magnarini *et al.* 2024). These striking deposit features extend to several kilometres in length, and give clues to the complex flow dynamics that is responsible for reducing the basal friction to very low values (Melosh 1979; Campbell 1989; Dade & Huppert 1998; Collins & Melosh 2003).

Forterre & Pouliquen (2001) showed that a rapid monodisperse dilute granular flow down an inclined plane could spontaneously develop a series of transverse ridges. From measurements of the longitudinal surface velocity and the mass flux, they inferred that the troughs were denser and moved downslope faster than the crests, with an average velocity of approximately 1.3 ms^{-1} and a solids volume fraction $\Phi \simeq 0.3$. Transverse surface velocities were approximately two orders of magnitude smaller, and transported grains from the crests to the troughs. This allowed Forterre & Pouliquen (2001) to infer the existence of longitudinal vortices that were aligned with the primary downslope flow direction. They argued that the instability was driven by collisions between particles and the base, which created a low-density basal layer that then convectively overturned, similar to Rayleigh–Bénard convection in fluids (Bodenschatz, Pesch & Ahlers 2000). Forterre & Pouliquen (2002) used the concept of granular temperature (random fluctuations in particle velocity) and kinetic theory for granular gases (Jenkins & Savage 1983; Goldhirsch 2003) to investigate the linear stability of a flowing layer that was 'heated' by tangential stress generated at the base. This analysis showed that kinetic theory is able to qualitatively explain the instability mechanism. However, longitudinal vortices were predicted at slope angles as low as $\zeta = 20°$, whereas the minimum angle that the instability was observed experimentally was 38°. Brodu, Richard & Delannay (2013) and Brodu *et al.* (2015) carried out discrete element method (DEM) simulations of high speed granular flows in a chute with frictional sidewalls. They found a rich variety of secondary flows that can have multiple stacked cells and oscillatory behaviour. Particle-size segregation also occurs in these flows (Neveu *et al.* 2022), but is driven by granular temperature gradients rather than by gravity and shear (Gray 2018; Trewhela, Ancey & Gray 2021).

As well as the dilute regime of Forterre & Pouliquen (2001), Börzsönyi *et al.* (2009) found that longitudinal vortices could also develop in a dense regime in which the solids volume fraction $\Phi \in [0.36, 0.57]$. In this case the ridges were denser and moved faster downstream than the troughs, and the vortices rotated in the opposite direction, i.e. the transverse surface velocity transported grains from the troughs to the ridges. Discrete element method simulations were used to simulate the flow. Dense longitudinal vortices were found for slope angles in the range $\zeta \in [34°, 39°]$. These revealed that there was a low-density basal 'boiling' layer beneath the ridges, which allowed the dense layer to flow faster downslope. This layer reminded the authors of the granular Leidenfrost effect in shaken systems (Eshuis *et al.* 2005). The DEM data were used to show that the friction μ and solids volume fraction Φ were functions of the inertial number I, i.e.

$$\mu = \mu(I), \qquad \text{and} \qquad \Phi = \Phi(I). \tag{1.1a,b}$$

https://doi.org/10.1017/jfm.2026.11311 Published online by Cambridge University Press

Here, the generalised compressible inertial number (GDR-MiDi 2004; Jop *et al.* 2006)

$$I = \frac{d||\boldsymbol{D}'||}{\sqrt{p/\rho_*}} \tag{1.2}$$

is defined in terms of the grain diameter d, the intrinsic particle density ρ_*, the pressure p and the second invariant of the deviatoric strain rate, $\boldsymbol{D}'$, as

$$||\boldsymbol{D}'|| = \sqrt{\frac{1}{2}\mathrm{tr}((\boldsymbol{D}')^2)}, \qquad \text{where} \qquad \boldsymbol{D}' = \boldsymbol{D} - \frac{1}{3}\mathrm{tr}(\boldsymbol{D})\boldsymbol{1}, \tag{1.3a,b}$$

and $\boldsymbol{1}$ is the unit tensor. The strain rate, $\boldsymbol{D} = (\boldsymbol{L} + \boldsymbol{L}^T)/2$, is defined in terms of the velocity gradient $\boldsymbol{L} = \boldsymbol{\nabla u}$ and its transpose. Although the functions $\Phi(I)$ and $\mu(I)$ collapsed the steady-state DEM data, the friction had a maximum at $I = 0.7$, instead of asymptoting to a constant at large I, or increasing monotonically. Such a decreasing dependence is potentially problematic, because granular rheologies with a rigid dependence of the friction on I are mathematically ill posed (Barker *et al.* 2015, 2017; Heyman *et al.* 2017*b*; Schaeffer *et al.* 2019). Dilation can also drive secondary flows in very slow flows, such as in the gap between two annular cylinders and in a split bottom cell (Krishnaraj & Nott 2016; Dsouza & Nott 2021).

The incompressible $\mu(I)$ rheology (GDR-MiDi 2004; Jop *et al.* 2006; Barker *et al.* 2015; Barker & Gray 2017) has been generalised to incorporate first and second normal stress differences (McElwaine *et al.* 2012; Srivastava *et al.* 2021; Kim & Kamrin 2023). This is achieved by assuming that the granular material is a second-order Rivlin–Erickson fluid (Truesdell 1977; Truesdell & Noll 2004) in which the Cauchy stress

$$\boldsymbol{\sigma} = -p\boldsymbol{1} + \frac{\mu_1(I)p}{||\boldsymbol{D}||}\boldsymbol{D} - \frac{\mu_2(I)p}{||\boldsymbol{D}||^2}\left(\boldsymbol{D}^2 - \frac{1}{3}\mathrm{tr}(\boldsymbol{D}^2)\boldsymbol{1}\right) - \frac{\mu_3(I)p}{||\boldsymbol{D}||^2}\mathring{\boldsymbol{D}}, \tag{1.4}$$

where the co-rotational, or Jaumann, derivative

$$\mathring{\boldsymbol{D}} = \dot{\boldsymbol{D}} - \boldsymbol{W}\boldsymbol{D} + \boldsymbol{D}\boldsymbol{W}, \tag{1.5}$$

is defined in terms of the material derivative $\dot{\boldsymbol{D}} = \partial \boldsymbol{D}/\partial t + (\boldsymbol{u} \cdot \boldsymbol{\nabla})\boldsymbol{D}$ and spin tensor $\boldsymbol{W} = (\boldsymbol{L} - \boldsymbol{L}^T)/2$. Since this rheology reduces to the incompressible $\mu(I)$-rheology when the functions μ_2 and μ_3 are zero, there may still be an issue with ill posedness. However, when μ_2 is non-zero, Gadal, Johnson & Gray (2026) showed that for shallow steady-state flows in a laterally curved channel, the second normal stress differences (i.e. between the slope normal and cross-slope directions) lead to a bowing up of the surface and the formation of two counter-rotating secondary vortices that transport material towards the central ridge along the flow surface. Second normal stress differences are therefore sufficient to generate secondary flows even in the absence of dilatation, but they may also act in combination with it, and potentially enhance the circulation.

D'Ortona & Thomas (2020) and D'Ortona *et al.* (2025) investigated a mixture of light and dense particles of the same size. By initially placing all the dense particles on top of the light grains and then inclining the chute, they observed a granular Raleigh–Taylor instability in DEM simulations and experiments. The flow destabilised into a series of plumes that allowed the dense particles to sink to the base and the light particles to rise to the surface of the flow. The plumes aligned with the downslope motion, creating a transverse instability in which light and dense plumes momentarily formed alternating stripes that were oriented in the downslope direction. Ultimately, the light particles found a stable equilibrium adjacent to the surface of the flow, so the density

https://doi.org/10.1017/jfm.2026.11311 Published online by Cambridge University Press

stripes only formed transiently and then decayed away. However, they also investigated mixtures of large–dense and small–light particles, and showed that these could also generate self-sustaining secondary vortices, which they termed a self-induced Raleigh–Taylor instability. Essentially, particle-size segregation (Gray 2018) seeks to drive the large particles to the surface of the flow and the small particles to the base, but when the large dense particles reach sufficient concentration the dense surface layer becomes unstable and overturns hydrodynamically. In this scenario, a series of continuously overturning plumes of large–dense and small–light particles forms that are also oriented with the downslope direction and form surface stripes that do not decay. This is a very subtle mechanism that relies on the density difference of the particles. In particular, D'Ortona & Thomas (2020) showed that if the density of the large and small particles were the same no stripes formed in their experiments.

This paper shows that particles that differ in size, but not density, can still form stripes, if there is an underlying secondary flow. In particular, particle-size segregation can help to reveal the existence of secondary flow, even when it is difficult to measure experimentally. A series of experiments are performed in § 2, which are in the dense flow regime described by Börzsönyi *et al.* (2009). One of the experiments releases a size bi-disperse mixture of differently coloured large and small particles (of the same bulk density) on a steep slope, and allows it to rapidly deposit on a shallow slope, preserving the stripes that formed during the flow. This is analogous to what happens in nature in some large run-out landslides, where transverse flow bands and ridges may extend longitudinally for several kilometres and have subtle compositional differences (Shreve 1966; Post 1967; McSaveney 1978; Dufresne & Davies 2009; Magnarini *et al.* 2019, 2024). The high mobility of these flows has often been ascribed to an underlying layer of ice (Blasio 2011), but Magarini *et al.* (2021) identified such features on the Moon, which has been ice free throughout its history. In contrast, Campbell (1989) used DEM simulations to show that long runout can be a purely granular phenomenon. As grains avalanche downslope, a dilute layer can form at the base, which supports the overburden and allows it to flow with greatly reduced friction. This is essentially the same granular Leidenfrost effect (Eshuis *et al.* 2005) that Börzsönyi *et al.* (2009) saw in their DEM simulations of dense secondary vortices, which suggests that the reduced friction and formation of secondary vortices may go hand in hand.

Although significant progress has been made in understanding the granular Leidenfrost effect, the formation of secondary vortices and the associated reduced friction in DEM simulations, there is currently no continuum theory that can simultaneously model all these effects. This paper therefore focusses on how a continuum model of particle-size segregation combines with the assumed existence of secondary vortices to generate stable surface stripes. A conceptual model is introduced in § 3, the governing equations are given § 4 and these are solved numerically in § 5. A steady-state exact solution is constructed in § 6 and this is used to investigate the complex three-dimensional large- and small-particle paths in § 8.

2. Experimental observations

2.1. *Curved chute experiment*

In order to investigate the process of longitudinal stripe formation, experiments are performed on a curved chute that initially accelerates the granular material downslope and then gradually brings it to rest to form a thin deposit, as shown in figures 1–4, as well as movies 1 and 2, available at https://doi.org/10.1017/jfm.2026.11311. The chute has no

https://doi.org/10.1017/jfm.2026.11311 Published online by Cambridge University Press



Figure 1. A photograph of the curved experimental chute, which consists of a flexible plane bent to produce a gradual slope angle change from $\zeta = 46°$ to the horizontal at its steepest point to $\zeta = 17°$ at its shallowest point. A hopper and two-gate system controls the inflow, the first gate is set at 25 mm and the second gate is used to start the flow. The bed was originally roughened with a monolayer of spherical turquoise glass ballotini (750–1000 μm), which was stuck down with double-sided tape. Over time this has partially worn off to reveal the white tape. A deposit formed by the release of a 30 : 70 mix of large green (200–250 μm) and small white (60–150 μm) glass ballotini is shown on the chute. Movies 1 and 2, available in the online supplementary material, show the complete experiment in real time and slow motion.

sidewalls and is made from a medium-density fibre board (2100 × 700 × 6.5 mm), which can be bent into the required shape. The board was covered with double-sided sticky tape and then a monolayer of spherical turquoise glass ballotini (750–1000 μm) was applied. Over time, some of these beads have worn off (figure 1), which has improved the ability of the experiment to generate stripes, and so the chute has not been recoated. The granular material consists of 30 : 70 mix of large green (200–250 μm) and small white (60–150 μm) spherical glass ballotini of the same bulk density. The grains are released from a double-gated hopper at the top of the chute. The first gate is fixed to a set height of

https://doi.org/10.1017/jfm.2026.11311 Published online by Cambridge University Press

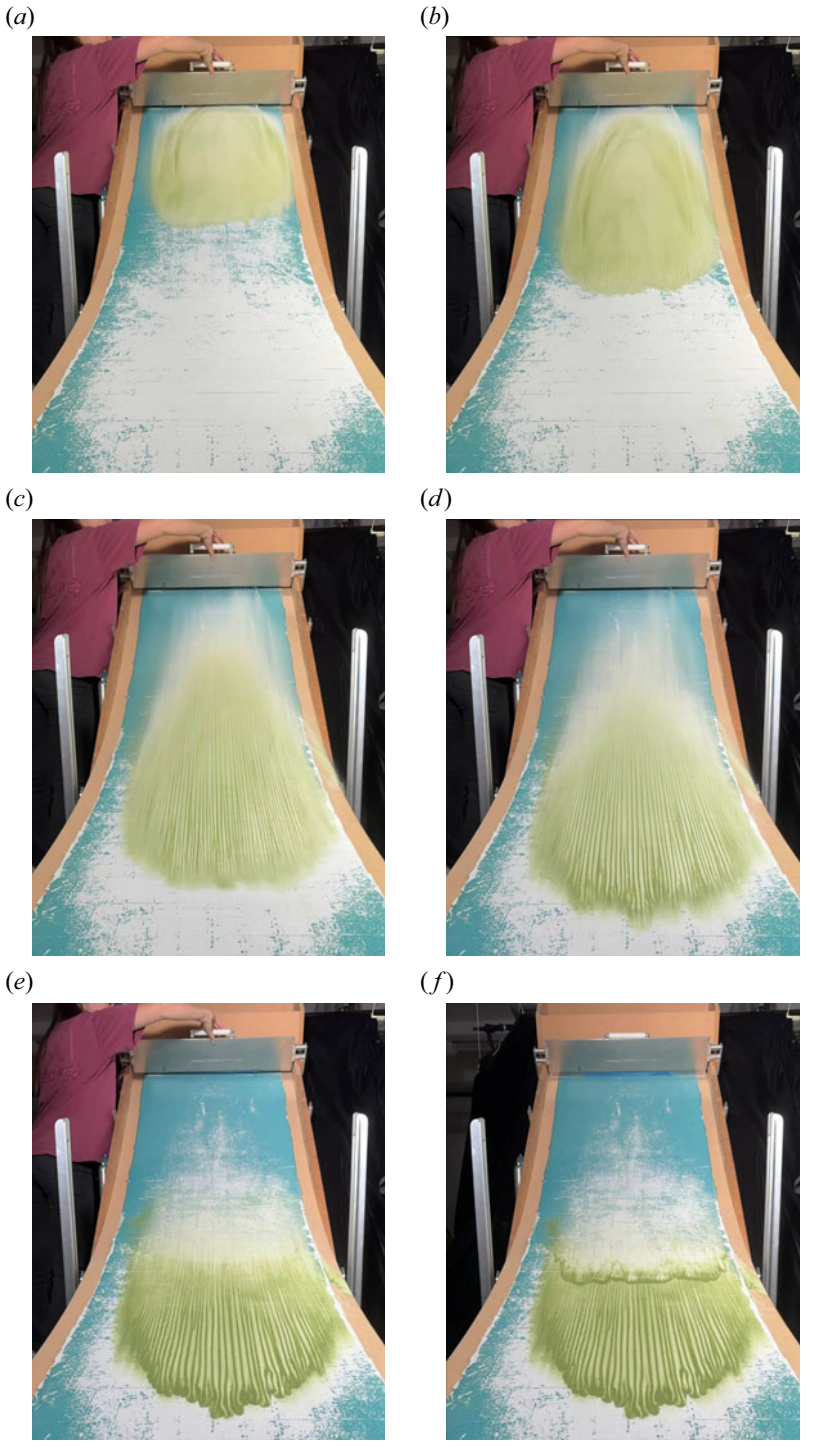


Figure 2. Photos showing the time-dependent evolution of the curved chute experiment shown in figure 1. The images are taken at (*a*) $t = 0.5$, (*b*) 0.76, (*c*) 1.22, (*d*) 1.24, (*e*) 2.04 and (*f*) 13.24 seconds after the gate is opened. Movies 1 and 2 in the online supplementary material show the complete experiment in real time and slow motion.

https://doi.org/10.1017/jfm.2026.11311 Published online by Cambridge University Press

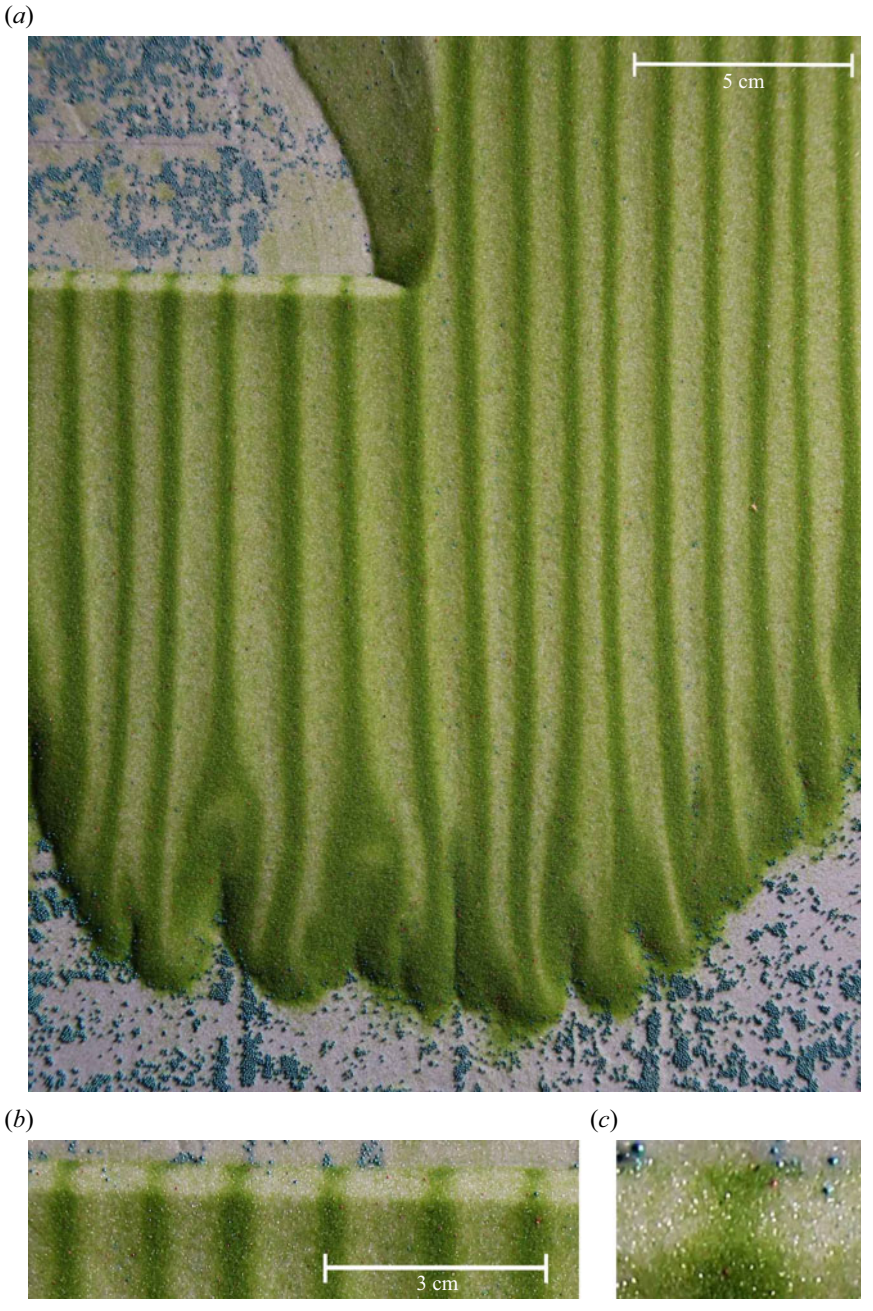
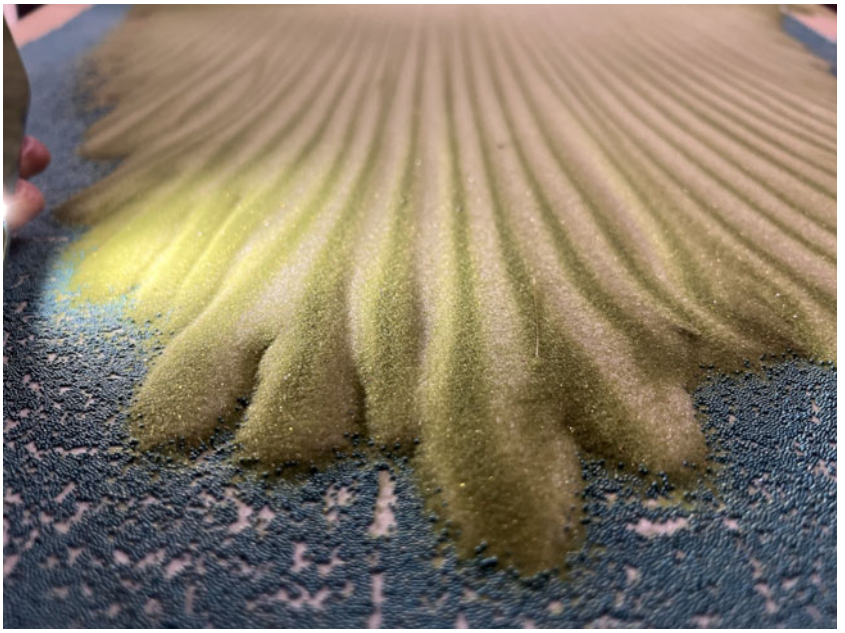


Figure 3. (*a*) An overhead photograph of the deposit formed by the release of a 30 : 70 mix of large green (200–250 μm) and small white (60–150 μm) glass ballotini on the curved chute in figures 1 and 2. The deposit consists of alternating green and white surface stripes, which have high concentrations of large and small particles, respectively. The stripes are terminated by a large-rich front that has just started to finger before arresting. In the upper left side of (*a*) material has been scraped away to reveal the internal structure (*b*), which shows that the large- and small-particle-rich stripes extend all the way from the surface to the base of the deposit. (*c*) A close-up photo of the vertical structure of a single large stripe.

https://doi.org/10.1017/jfm.2026.11311 Published online by Cambridge University Press

(*a*)



(*b*)

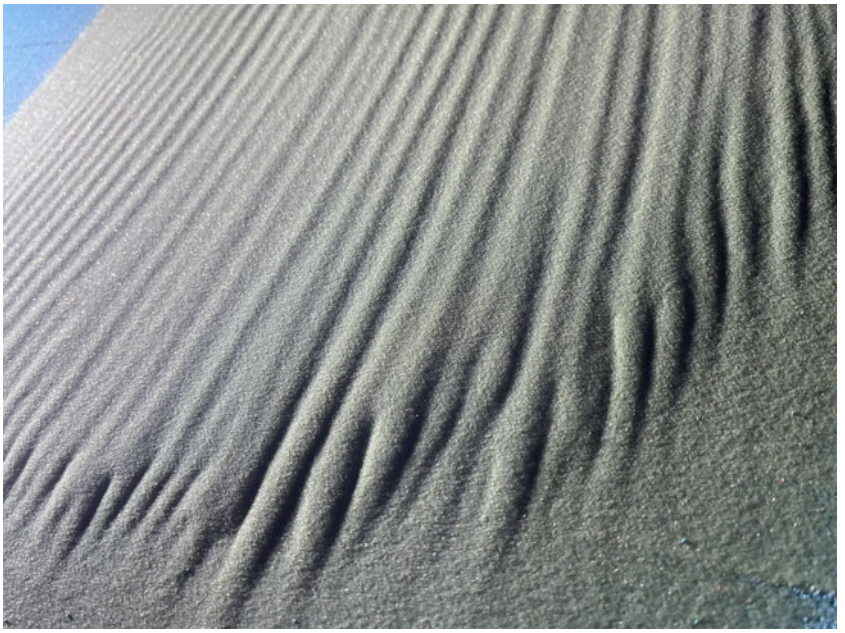


Figure 4. (*a*) A perspective photograph showing a similar deposit to that in figure 3, but with oblique lighting to highlight the subtly raised large-particle ridges in the deposit formed by the release of a 30 : 70 mix of large green (200–250 μm) and small white (60–150 μm) glass ballotini on the curved chute. (*b*) An obliquely lit photograph showing the deposited ridges in a monodisperse flow of large green ballotini on the same curved chute. Note that the oblique lighting makes the particles look grey.

https://doi.org/10.1017/jfm.2026.11311 Published online by Cambridge University Press

25 mm, to partially control the mass flux, while the second gate is used to release a mass of approximately 2 kg. This finite mass ensures that stripes are preserved in a sizeable part of the deposit (figure 1).

The initial charge of grains is placed in the centre of the hopper and the second gate is then opened. Figure 2, as well as movies 1 and 2, show the time-dependent evolution of the flow down the curved chute. At $t = 0.5$ s, when the grains are on the steepest 46° section of the chute, the flow spreads both longitudinally and laterally, and the surface appears a uniform shade of greeny white. It is not until $t = 0.76$ s that the first signs of the stripes emerge just behind the flow front as it transitions onto the shallow slope. The front itself appears slightly wavy and diffuse, and is whiter in colour suggesting that it may be richer in small particles. There are also a couple of stripes higher up, in the thinner regions at the sides, which initially spread out laterally. By $t = 1.22$ s, long linear alternating bands of green and white particles (i.e. the stripes) extend from the front to the tail of the flow. Near the front, there is some evidence of stripe formation and merging, but once a distinct wavelength has developed the stripes can be traced all the way to the back of the flow. The front is still somewhat diffuse, wavy and whiter than the main body of grains.

At $t = 1.24$ s the flow front reaches the decelerating part of the chute, where the slope angle reduces to $\zeta = 17°$. In this region large grains are segregated towards the flow surface and then sheared towards the flow front (Gray & Kokelaar 2010*b*; Johnson *et al.* 2012; Gray 2018). There is therefore a rapid transition to the development of a large-rich flow front, which feels more resistance to motion than the finer grained material behind, and the flow begins to finger just before it stops (Pouliquen, Delour & Savage 1997; Woodhouse *et al.* 2012; Baker, Johnson & Gray 2016*b*). By $t = 2.04$ s, the front of the avalanche has completely stopped and in the rear half of the flow there is a tiny shock wave that propagates back upslope bringing the remaining grains to rest. This thickens the flow and the depth of the large-rich surface layer, making the greener regions stand out more, which is consistent with the observations and model of Gray & Kokelaar (2010*a*,*b*) (see § 4.2). During this slowing phase, it is likely that the vortical circulation shuts off and the flow begins to transition to an inversely graded segregation pattern, with large grains on top of small. However, the flow comes to rest so quickly, within the banded section, that not that much segregation/diffusion occurs, allowing the stripes to be well preserved.

In the final phase of flow, some of the slowly moving material upstream of the shock wave is able to break through it and initiate small erosion-deposition waves that propagate relatively easily on the existing deposit (Edwards & Gray 2015; Rocha, Johnson & Gray 2019). In these waves, standard segregation is active and erosion-deposition wave fronts become rich in large particles, whilst the tails are almost pure fines. Note that, if the change in chute angle is too weak, or the flow volume is too large, erosion-deposition waves can completely rework the deposit, and destroy any evidence of stripe formation. In the current experiment the change in chute angle and the release volume have been optimised to ensure the stripes are preserved in the deposit. By $t = 13.24$ s these slowly propagating erosion-deposition waves have also come to rest to reveal the final deposit. It consists of a large-rich slightly fingered front (which only formed in the later stages of motion), a large region of well-preserved stripes immediately behind the front, which extends a long way upstream, and finally a heavily reworked scalloped tail section in which the stripes have been destroyed by erosion-deposition waves.

Figure 3(*a*) shows a close-up overhead view of the large-rich fingered flow front and the striped deposit behind it. Qualitatively it looks very similar to the Sherman rock avalanche deposit illustrated in figure 4 of Shreve (1966) and figure 6 of Post (1967). The stripes are remarkably evenly spaced, with a wavelength of approximately 12–13 mm between the centres of the large-rich bands. The large-rich bands themselves are slightly diffuse,

https://doi.org/10.1017/jfm.2026.11311 Published online by Cambridge University Press

but have a typical width of 2–4 mm at the surface. The white bands are wider, which is a direct reflection of the initial 30 : 70 mixing ratio. The deposit has subtly raised ridges that coincide with the large-rich bands, as shown by the obliquely lit photograph in figure 4(*a*). Figure 4(*b*) shows that similar ridges form even for a monodisperse flow of large green ballotini. This suggests that particle-size segregation is not the underlying cause of the vortical motion, but instead helps to make its effects visible. In the upper left corner of figure 3(*a*) a ruler has been used to cut the flow vertical downwards and scrape the upstream material backwards and away from the deposit to reveal the internal structure (figure 3*b*). The stripes extend all the way from the surface to the base of the flow, i.e. there are alternating vertical bands of almost pure large and pure small particles. The close-up view of a single large vertical stripe is shown in figure 3(*c*). The band is slightly wider at the top and bottom of the flow than in the middle. As shall be shown in this paper, such a particle-size distribution is consistent with existing mechanisms for particle-size segregation combined with streamwise secondary vortices in the bulk flow.

2.2. *Straight chute experiment*

Although the formation of stripes on the curved chute is striking, it is a complicated flow involving many processes. In order to simplify the system, experiments have also been performed on a straight 2.84 m long chute that is inclined at an angle $\zeta = 34.5°$ to the horizontal, and has glass sidewalls that are separated by a gap of 7.8 cm. The base is covered with the same spherical turquoise glass ballotini (750–1000 μm) as the curved chute (see right-hand side of figure 5*a*). A well-mixed sample of the same 30 : 70 mix of large green (200–250 μm) and small white (60–150 μm) glass ballotini (of the same bulk density) is released from a two-gate system. The first gate is set at 10 mm and maintains a steady uniform-depth inflow until the hopper runs out of material.

When the grains are released they flow rapidly down the chute as shown in the real time and slow motion overhead movies 3 and 4. The camera window is located between 2.15 and 2.55 m downslope. Stills of the movie are shown in figure 5 at a sequence of times measured from when the front first enters the camera window. In figure 5(*a*) the front is just propagating into view. It is somewhat diffuse, and there is a cloud of fine grained material at the front. The stripes appear just behind the front and are highly dynamic in their initial phase (figure 5*b*), bending and merging as they try to equilibrate themselves. By $t = 1.92$ s a quasi-steady-state striped pattern has established itself, with alternating bands of large (green) and small (white) material (figure 5*c*). There are five fully formed stripes in the centre of the channel, measured from centre to centre of adjacent large-rich bands, with wider fines-rich bands adjacent to the chute walls. The stripes are evenly spaced and are approximately 10 mm wide, which is slightly narrower than on the curved chute. While there is strong variation in composition across the chute, downstream gradients are generally very weak. There is, however, some slow drift of the bands and occasional intense pulses (figure 5*d*) with a sequence of waves that span the bands and travel rapidly down slope out of view. This generates a short-lived periodic flashing effect. As the material runs out of the hopper and the flow thins, the pattern changes from downstream oriented stripes to cross-slope oriented large-rich bands that propagate down slope. These are due to the formation of bidisperse roll waves (Viroulet *et al.* 2018).

A space–time plot derived from movie 3 is shown in figure 6(*a*). It clearly shows the fines-rich front flowing down the empty chute (horizontal grey lines for $t < 0.4$ s), which is followed by the highly dynamic region where the stripes begin to form. Simultaneous laser height measurements (figure 6*b*) indicate that this dynamic regime corresponds to when the flow is thickening. Between $t = 0.4$ and 1.9 s, when the flow is thinner,

https://doi.org/10.1017/jfm.2026.11311 Published online by Cambridge University Press

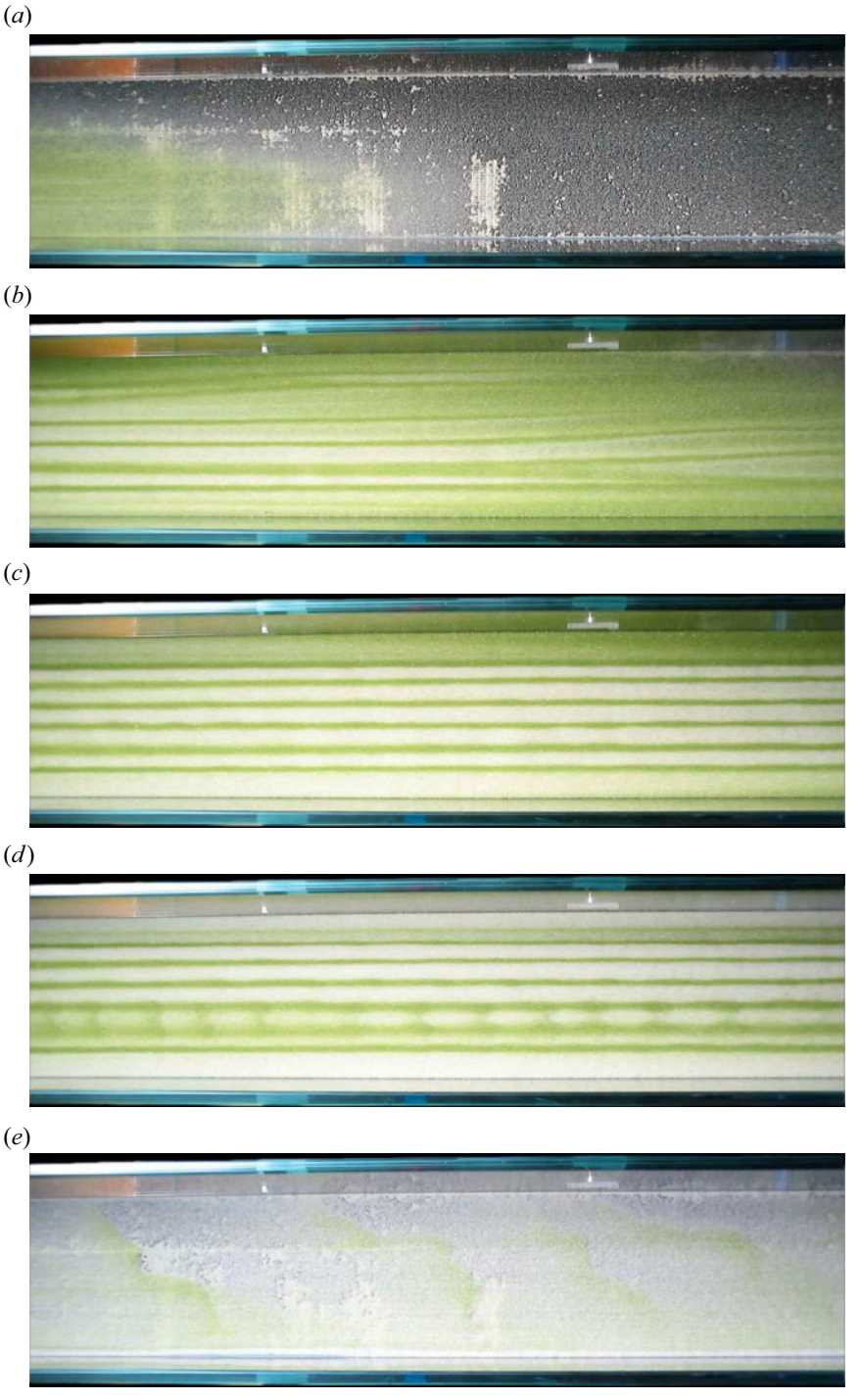


Figure 5. Overhead photographs (*a–e*) taken in a window that lies 2.15–2.55 m down the chute, showing the flow of a 30 : 70 mix of large green (200–250 μm) and small white (60–150 μm) glass ballotini on a chute inclined at $\zeta = 34.5°$ to the horizontal. The photos are taken at $t = 0.28$, 1, 1.92, 5.94 and 12.58 s after the avalanche first enters the camera window. The complete time-dependent evolution is shown in real time and slow motion in movies 3 and 4 .

https://doi.org/10.1017/jfm.2026.11311 Published online by Cambridge University Press

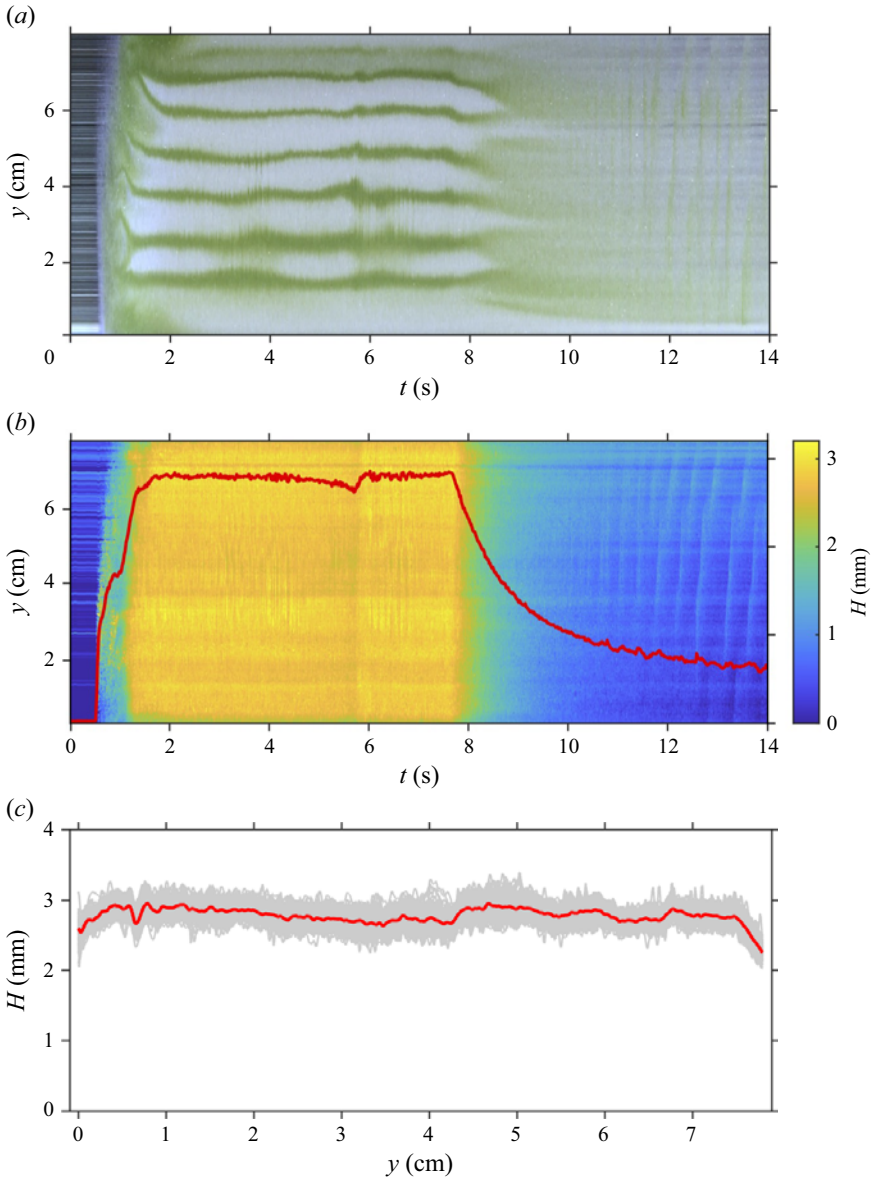


Figure 6. (*a*) An overhead space–time plot of the straight-chute experiment showing the development of the stripes. It is created from movie 3 by stacking a series of pixel columns taken at approximately 2.55 m down the chute. (*b*) A corresponding space–time plot of laser height measurements H across the chute at approximately 2.6 m downslope. The superposed red line indicates the average height as a function of time using the colour bar as an axis. (*c*) The flow thickness across the chute between times $t = 1$ and 7 s when the quasi-steady stripes have formed. The grey region shows all the data, while the red line shows the average flow thickness.

the surface images show that the flow appears to have more stripes, but as the flow thickens the bands coarsen and equilibrate (figure 6*a*). There then follows a sustained period of approximately constant depth flow $t \in [1.8, 7.7]$ s, with little variation across the chute, except near the sidewalls where the flow bulges slightly upwards (figure 6*b*,*c*). During this phase of flow the stripes are relatively stable, with six large-rich flow bands that deviate only slightly in width and position. As the material runs out of the hopper, and the flow

https://doi.org/10.1017/jfm.2026.11311 Published online by Cambridge University Press

begins to thin again, between $t = 7.7$ and 8.5 s, the space–time plot shows that the flow tries to develop more stripes again (figure 6*a*). However, the stripes become diffuse and peter out by $t = 10$ s and there is a transition to the formation of bidisperse roll waves that propagate downslope, and have large-rich cross-slope bands that correlate with the peak flow heights as seen by Viroulet *et al.* (2018).

The laser height measurements (figure 6*c*) indicate that during the uniform-depth flow phase the average depth is approximately 2.7 mm and there are no obvious bulges or ridges that correlate with the position of the large- and small-particle bands, although the large-rich bands are subtly raised in the deposit (see figure 4*a*). The absence of obvious ridges during flow may be due to (i) the relatively low inclination of the chute, (ii) differential dilation of the two species and/or (iii) simply that the ridges are of sufficiently small amplitude that they are lost in the measurement noise, especially if there is some lateral drift in their position. Note that in monodisperse flows, well-defined ridges during flow were observed at significantly higher inclinations and only for specific hopper openings (Börzsönyi *et al.* 2009). Our premise here is that segregation is helping to reveal the presence of secondary vortices, rather than being the root cause of them. This is supported by the fact that subtly raised ridges are observed in the deposit of a monodisperse flow on the same chute (see figure 4*b*).

In our conceptual model for the flow, which will be discussed shortly in detail in § 3, it is argued that each stripe consists of two counter-rotating secondary vortices that are oriented in the downslope direction. Since the width of each stripe is approximately 10 mm, it follows that the height-to-width aspect ratio of each vortex is approximately 1.85. Surface velocities have also been measured during the uniform-depth phase by tracking individual tracer particles. Typical downslope velocities are of the order of $1.38\,\mathrm{m\ s^{-1}}$, which are much larger than any cross-slope velocity components. The fact that the flow is rapid and dense, and the particles are of the same bulk density, suggests that the secondary vortices correspond to the dense regime observed in monodisperse flows by Börzsönyi *et al.* (2009), i.e. particle-size segregation is not causing the secondary vortices, but responds sensitively to their presence and helps to reveal their existence.

3. Conceptual model for the formation of steady stripes

The experimental observations in § 2 require a conceptual model to explain them. This is because in a dense dry size-bidisperse granular mixture that is flowing down a slope, one would normally expect large particles to be squeezed upwards, towards the surface, and small particles to percolate downwards, towards the base (Gray 2018; Trewhela *et al.* 2021; Barker *et al.* 2021). Instead, a series of size-segregated stripes (or bands) rapidly form that are oriented parallel to the downslope direction (see figure 7*a*). Although this appears counter-intuitive, it can be explained within the existing particle-size segregation framework.

In the simplest case, one can imagine that the flow is of uniform depth, and the downslope velocity component u has a profile through the flow depth z, i.e. $u = u(z)$. For a dense dry granular flow with no slip at the base this would be a Bagnold velocity profile (Silbert, Landry & Grest 2003; GDR-MiDi 2004; Jop, Forterre & Pouliquen 2005; Gray & Edwards 2014), i.e.

$$u = u^*\left(1 - \left(1 - \frac{z}{H}\right)^{\frac{3}{2}}\right), \tag{3.1}$$

where $z = H$ is the free-surface height and u^* is a typical downslope surface velocity magnitude. This is illustrated schematically in figure 7(b). The magnitudes of the

https://doi.org/10.1017/jfm.2026.11311 Published online by Cambridge University Press

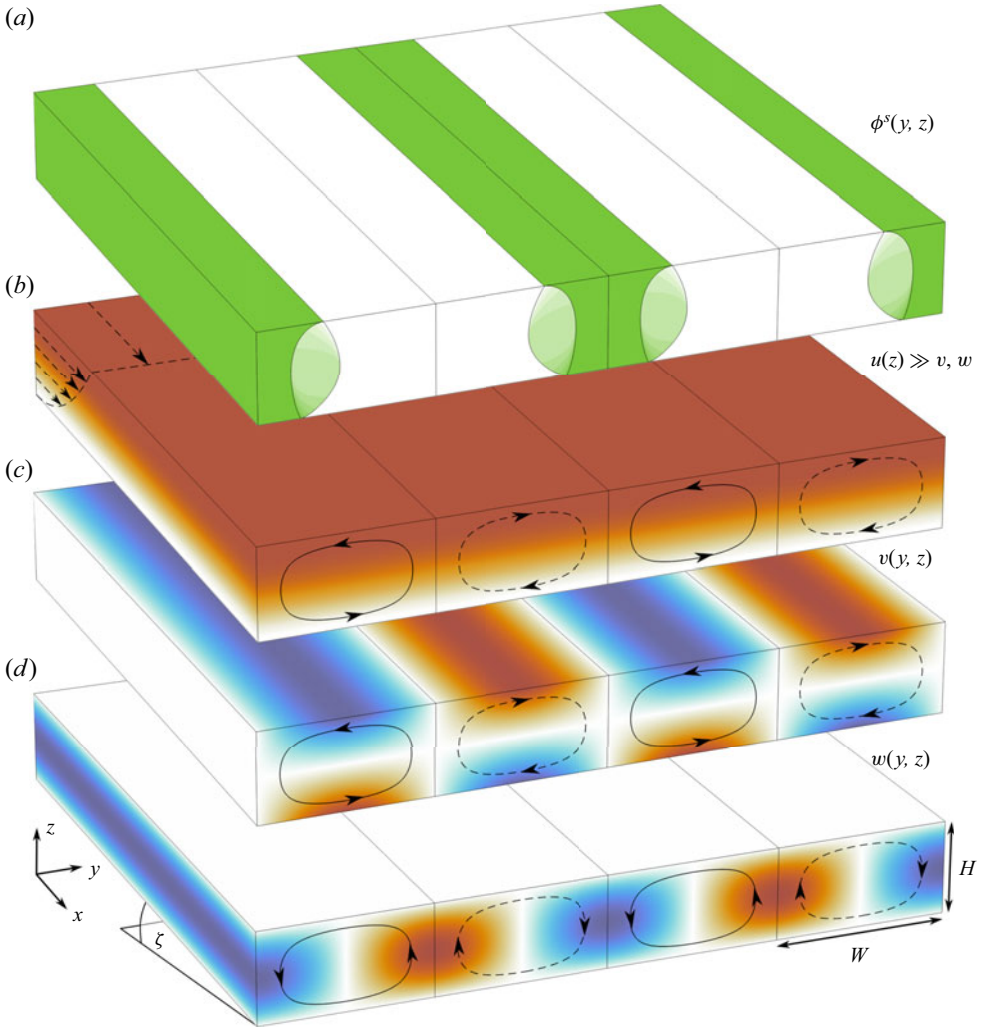


Figure 7. Perspective view of a simple conceptual model for the formation of two steady-uniform stripes measured from the centre of adjacent large-rich bands. A coordinate system $Oxyz$ is defined on a plane that is inclined at an angle ζ to the horizontal. The x axis is oriented down the slope, the y axis lies across the slope and the z axis is parallel to the upward pointing normal. The velocity field has components $\boldsymbol{u} = (u, v, w)$ in each of these directions. (*a*) The small-particle concentration $\phi^s = \phi^s(y, z)$ is assumed to be independent of x. Regions of pure large (green) and pure small (white) particles form, which are separated by breaking-size-segregation waves (light green) (Thornton & Gray 2008; Gray & Ancey 2009; Edwards *et al.* 2023). These allow large and small grains to be recirculated upwards/downwards and form closed recirculating loops. (*b*) The downslope velocity $u(z) \gg v, w$ is dominant. For a dry granular flow this would typically be given by a Bagnold profile (3.1). Panels (*c*,*d*) show that there are four counter-rotating secondary vortices oriented in the downslope direction x. A secondary vortex that is rotating anticlockwise/clockwise is drawn with solid/dashed arrowed line. The vortices are assumed to have a height H and width W. The cross-slope and normal velocity components (v, w) are functions of y and z only. The pure phases of large particles accumulate in the downwelling part of the flow, while the pure small regions develop in the upwelling part.

cross-slope velocity v and normal velocity w are typically much smaller than the downslope velocity u. The DEM simulations performed by Börzsönyi *et al.* (2009) suggest that the maximum magnitude of cross-slope surface velocities is approximately 4 % of the downslope surface velocity. It follows that the gradient $\partial u/\partial z$ determines the dominant

https://doi.org/10.1017/jfm.2026.11311 Published online by Cambridge University Press

shear rate, and hence the magnitude of the segregation velocity (Trewhela *et al.* 2021; Edwards *et al.* 2023; Maguire *et al.* 2024). The key to the stripe formation is that there are also a series of counter-rotating secondary vortices, whose axes of rotation are oriented in the downslope direction, as shown in figure 7(*c*,*d*). Their existence is hard to detect in monodisperse experiments and DEM simulations (Gadal *et al.* 2026), because v and w are so much smaller than u. Many apparently mundane flows may therefore have secondary recirculation!

The basic idea is that each stripe (measured between the centres of the adjacent large-particle bands) consists of a pair of counter-rotating secondary vortices. Even though the secondary recirculation is small compared with the typical downstream velocities, it is very significant. This is because, if one imagines an inversely graded interface between large (above) and small particles (below), then in the absence of diffusion the vortical motion will rotate the interface around with the flow, until it becomes vertical and breaks. Large particles that have been advected to the base of the flow and dragged underneath small grains, will then segregate to the top of the flow again, while small particles that have been advected to the top and above large grains will percolate downwards. A series of breaking-size-segregation waves, that are aligned with the flow direction, will therefore form, enabling both the large and small particles to be recirculated (Thornton & Gray 2008; Gray & Ancey 2009; Edwards *et al.* 2023). This allows a banded structure to form, with pure large particles in the downwelling sections of the secondary vortices, pure small particles in the upwelling sections and a breaking-size-segregation wave in between the two, as shown in figure 7(*a*). The detailed structure of these waves and how the particles recirculate will be investigated in detail shortly.

When viewed from above, the combination of particle segregation and the secondary recirculation produce a series of alternating bands of large and small particles that align with the downstream flow direction. This conceptual picture, which is shown schematically in figure 7(*a*), is consistent with all the experimental observations in § 2. In particular, the stripes extend all the way through the flow depth, as observed in the sectioned deposit in figure 3(*b*). Moreover, the fact that a breaking-size-segregation wave separates the large- and small-particle-rich regions implies that the pure large regions will be slightly wider at the top and bottom of the flow, than in the middle, which is consistent with figure 3(*c*) and is sketched schematically in figure 7(*a*).

4. Governing equations

It is of interest to show that existing theories for particle-size segregation can model the formation of stripes, provided that secondary vortices are assumed to exist.

4.1. *The segregation-advection equation*

Consider a bidisperse mixture of large and small particles that is flowing down a chute inclined at a fixed angle ζ to the horizontal. A Cartesian coordinate system $Oxyz$ is defined with the x-axis pointing in the downslope direction, the y-axis in the cross-slope direction and the z-axis normal to the slope as illustrated in figure 7. All the particles are assumed to have the same intrinsic density and the prescribed bulk velocity field $\boldsymbol{u} = u\boldsymbol{i} + v\boldsymbol{j} + w\boldsymbol{k}$ has components (u, v, w) in the directions of the downslope, cross-slope and normal unit vectors $\boldsymbol{i}$, $\boldsymbol{j}$ and $\boldsymbol{k}$. The large- and small-particle concentrations per unit granular volume are ϕ^l and ϕ^s, respectively. These sum to unity

$$\phi^l + \phi^s = 1, \tag{4.1}$$

https://doi.org/10.1017/jfm.2026.11311 Published online by Cambridge University Press

and satisfy a pair of segregation-advection equations (Gray & Thornton 2005; Gray & Ancey 2011; Gray 2018)

$$\frac{\partial \phi^l}{\partial t} + \nabla \cdot (\phi^l \boldsymbol{u}) + \nabla \cdot (f_{ls} \phi^l \phi^s \boldsymbol{e}) = 0, \tag{4.2}$$

$$\frac{\partial \phi^s}{\partial t} + \nabla \cdot (\phi^s \boldsymbol{u}) - \nabla \cdot (f_{ls} \phi^s \phi^l \boldsymbol{e}) = 0, \tag{4.3}$$

where f_{ls} is the segregation velocity magnitude, $\boldsymbol{e}$ is a unit vector oriented in the direction that large particles segregate, ∇ is the gradient operator and $\cdot$ is the dot product. Motivated by the relatively sharp segregation observed in experiments in § 2, diffusion is neglected in this simple formulation. The time rate of change of the large- and small-particle concentrations therefore evolves due to advection by the bulk flow field and particle segregation parallel to $\boldsymbol{e}$. Note that when (4.2) and (4.3) are added together, the summation condition (4.1) implies that the bulk velocity field $\boldsymbol{u}$ is incompressible

$$\nabla \cdot \boldsymbol{u} = 0. \tag{4.4}$$

The summation constraint (4.1) can be used to eliminate one of the concentrations. For instance, eliminating the large-particle concentration implies that the uncoupled form of the small-particle segregation-advection equation, (4.3), is

$$\frac{\partial \phi^s}{\partial t} + \nabla \cdot (\phi^s \boldsymbol{u}) - \nabla \cdot \Big(f_{ls} \phi^s (1 - \phi^s) \boldsymbol{e} \Big) = 0. \tag{4.5}$$

This is subject to a no-flux condition on the boundary of the avalanche. Gray & Thornton (2005) showed that this is equivalent to the condition that either

$$\phi^s = 0 \quad \text{or} \quad \phi^s = 1 \tag{4.6}$$

on the boundary of the avalanche.

The direction of segregation $\boldsymbol{e}$ is usually assumed to be aligned with the direction of gravitational acceleration $\boldsymbol{g}$. This is consistent with the idea that small particles percolate downwards under the action of gravity. However, the process in which large particles are squeezed towards the surface by force imbalances (Savage & Lun 1988) may instead align with the pressure gradient, and $\boldsymbol{e}$ may therefore be normal to the chute. The precise orientation of the segregation direction is therefore still open to some interpretation, although it is not important for the purposes of this paper.

4.2. *Uniform stripes in the downslope direction*

The straight chute experiment in § 2.2 shows that a series of stripes form that are weakly dependent of the downstream coordinate x. This suggests that a useful simplification is to assume that the large- and small-particle concentrations are spatially uniform in the downstream direction, i.e. $\phi^l = \phi^l(y, z, t)$ and $\phi^s = \phi^s(y, z, t)$. Since, the velocity field $\boldsymbol{u}$ is also assumed to be independent of x, the incompressibility condition (4.4) reduces to

$$\frac{\partial v}{\partial y} + \frac{\partial w}{\partial z} = 0. \tag{4.7}$$

Assuming that the segregation direction $\boldsymbol{e}$ does not have a cross-slope component, the small-particle segregation-advection equation, (4.5), becomes

$$\frac{\partial \phi^s}{\partial t} + \frac{\partial}{\partial y}(\phi^s v) + \frac{\partial}{\partial z}(\phi^s w) - \frac{\partial}{\partial z}\Big(q \phi^s (1 - \phi^s) \Big) = 0, \tag{4.8}$$

https://doi.org/10.1017/jfm.2026.11311 Published online by Cambridge University Press

where the normal component of the segregation velocity is

$$q = f_{ls}\, \boldsymbol{e} \cdot \boldsymbol{k}. \tag{4.9}$$

The assumption of uniformity in the downslope direction implies that (4.8) appears to be independent of the downslope velocity u. In general, the segregation velocity q is linearly proportional to shear rate $\dot{\gamma} = 2||\boldsymbol{D}||$, inversely proportional to the pressure and has further dependencies on the particle sizes, the particle-size ratio and the local concentrations of the two particle species (Trewhela *et al.* 2021; Maguire *et al.* 2024). The downslope velocity therefore enters (4.8) indirectly through its gradient $\partial u/\partial z$. Since $\partial u/\partial z$ is much larger than any of the other strain-rate components (related to the secondary recirculation), it provides the dominant contribution that sets the magnitude of q. For simplicity q is assumed to be a fixed constant in this paper, although, in general, there is some weak dependence of q on z in a Bagnold flow, which subtly changes the structure of the breaking-size-segregation waves that form (Edwards *et al.* 2023). Assuming that q is constant has the advantage that it allows us to investigate the qualitative dependence of the solutions over the complete parameter space, and derive exact solutions to the equations that yield considerable insight.

4.3. *Parameterisation of the secondary vortices*

The secondary vortices are not solved for in this paper. Instead they are parameterised in a very simple way, by assuming that they are rectangular in shape and have an incompressible velocity field of the form

$$v = \Omega \sin\left(\frac{\pi y}{W}\right)(2z - H), \qquad 0 \leqslant z \leqslant H, \qquad mW \leqslant y \leqslant nW, \tag{4.10}$$

$$w = -\left(\frac{\Omega \pi}{W}\right) \cos\left(\frac{\pi y}{W}\right) z(z - H), \qquad 0 \leqslant z \leqslant H, \qquad mW \leqslant y \leqslant nW, \tag{4.11}$$

where Ω sets the rotation rate, H is the cell depth and W its width. The integers m and $n > m$ determine the lateral extent of the cells. In general, the flow has $n-m$ vortices, with adjacent vortex cells that counter-rotate. Since each complete stripe consists of two counter-rotating vortices, the flow will have $(n-m)/2$ stripes, as shown in figure 7.

4.4. *Non-dimensional variables*

It is useful to introduce non-dimensional variables by using the scalings

$$(y, z) = H(\tilde{y}, \tilde{z}), \qquad (v, w) = \Omega H(\tilde{v}, \tilde{w}), \qquad t = (H/q)\tilde{t}, \tag{4.12a,b,c}$$

where the non-dimensional variables are denoted by a tilde. Note, the velocity scale ΩH is based on a typical rotational velocity magnitude, and the time scale H/q is based on a typical time for segregation to occur. Substituting these implies that the incompressibility condition (4.7) and the small-particle segregation-advection equation, (4.8), become

$$\frac{\partial \tilde{v}}{\partial \tilde{y}} + \frac{\partial \tilde{w}}{\partial \tilde{z}} = 0, \tag{4.13}$$

$$\frac{\partial \phi^s}{\partial \tilde{t}} + \frac{1}{\Lambda}\frac{\partial}{\partial \tilde{y}}(\phi^s \tilde{v}) + \frac{1}{\Lambda}\frac{\partial}{\partial \tilde{z}}(\phi^s \tilde{w}) - \frac{\partial}{\partial \tilde{z}}\Big(\phi^s(1 - \phi^s)\Big) = 0, \tag{4.14}$$

where the non-dimensional parameter

$$\Lambda = \frac{q}{H\Omega}, \tag{4.15}$$

https://doi.org/10.1017/jfm.2026.11311 Published online by Cambridge University Press

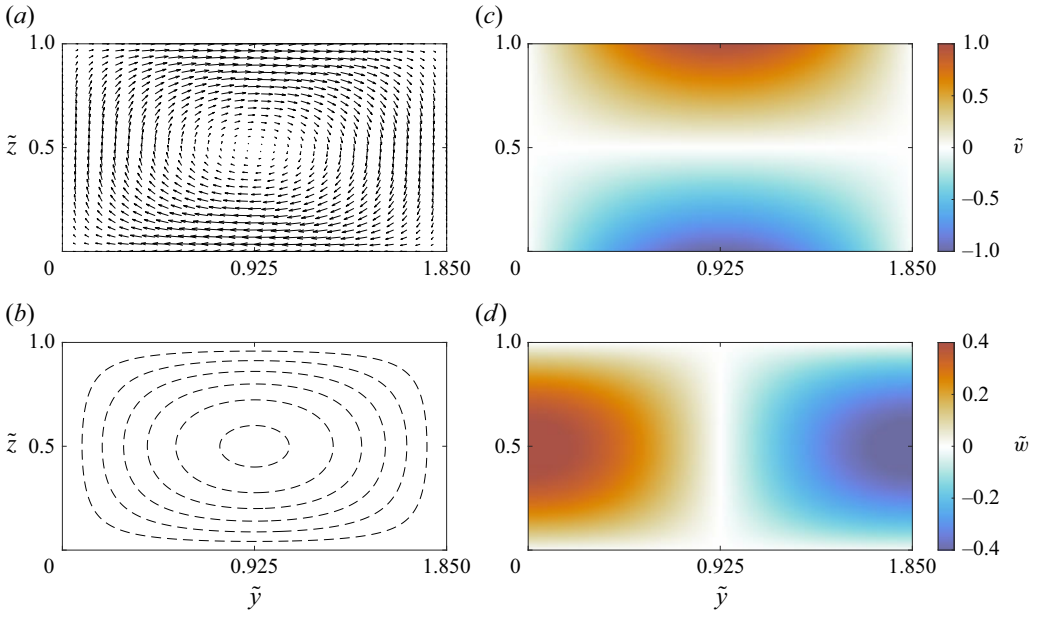


Figure 8. A single clockwise rotating steady-state secondary vortex in the $(\tilde{y}, \tilde{z})$ plane of width $\tilde{W} = 1.85$. (*a*) A quiver plot of the cross-slope and normal velocities, (*b*) the associated streamfunction and (*c*,*d*) contour plots of the individual velocity components given by (4.16)–(4.17).

is the ratio of a typical segregation velocity q to a typical secondary-vortex velocity $H\Omega$. The scalings (4.12) imply that the non-dimensional velocity field becomes

$$\tilde{v} = \sin\left(\frac{\pi\tilde{y}}{\tilde{W}}\right)(2\tilde{z} - 1), \qquad 0 \leqslant \tilde{z} \leqslant 1, \qquad \tilde{W}m \leqslant \tilde{y} \leqslant \tilde{W}n, \tag{4.16}$$

$$\tilde{w} = -\left(\frac{\pi}{\tilde{W}}\right)\cos\left(\frac{\pi\tilde{y}}{\tilde{W}}\right)\tilde{z}(\tilde{z} - 1), \qquad 0 \leqslant \tilde{z} \leqslant 1, \qquad \tilde{W}m \leqslant \tilde{y} \leqslant \tilde{W}n, \tag{4.17}$$

where $\tilde{W}$ is the non-dimensional vortex cell width. The non-dimensional velocity field in a single clockwise-rotating secondary vortex is plotted in figure 8. It uses the same contour scale as in figure 7(*c*,*d*), so the symmetry of the entire velocity field becomes apparent.

In order to solve for the small-particle concentration it is necessary to set the initial concentration

$$\phi^s(\tilde{y}, \tilde{z}, 0) = \phi_0^s(\tilde{y}, \tilde{z}), \qquad (\tilde{y}, \tilde{z}) \in [\tilde{W}m, \tilde{W}n] \times [0, 1], \tag{4.18}$$

where ϕ_0^s is the initial small-particle concentration distribution. Along the surface and base of the flow ($\tilde{z} = 0, 1$) the no flux conditions (4.6) imply that

$$\phi^s = 0, \quad \text{or} \quad \phi^s = 1 \quad \text{on} \quad \tilde{z} = 0, 1, \tag{4.19}$$

and the no-flux condition is trivially satisfied on the vortex interfaces.

5. Time-dependent numerical simulations

5.1. *Numerical method*

The segregation-advection equation, (4.14), is solved with the high-resolution central scheme of Kurganov & Tadmor (2000) using a second-order Runge–Kutta time-stepping

https://doi.org/10.1017/jfm.2026.11311 Published online by Cambridge University Press

method. The non-dimensional width of the secondary vortices is assumed to be

$$\tilde{W} = 1.85, \tag{5.1}$$

which is consistent with the experimental observations in § 2. The computations are performed in a single clockwise-rotating secondary-vortex cell defined in the region $(\tilde{y}, \tilde{z}) \in [0, 1.85] \times [0, 1]$ non-dimensional units. The numerical method implicitly assumes that $\partial \phi^s / \partial y = 0$ along the boundaries with the neighbouring vortices at $\tilde{y} = 0, 1.85$. The non-dimensional velocity field (4.16)–(4.17) is prescribed (see figure 8).

5.2. *Evolution from an inversely graded initial state*

A 30 : 70 mixture of large and small particles is initially assumed to be sharply segregated with large particles on top of the small grains, as shown in figure 9(*a*). In the absence of secondary recirculation, this would be a natural stable steady-state solution. However, when the recirculation is non-zero, the velocity field rotates the interface clockwise with the flow, causing it to steepen. Large particles therefore become concentrated in the downwelling section on the right-hand side of the cell (as shown in figure 9*b*), while small particles become concentrated in the upwelling region on the left. At approximately $\tilde{t} = 1.5$ non-dimensional units, the interface between large and small particles becomes vertical in the interior of the flow, and breaks to form a new structure that is known as a breaking-size-segregation wave (Thornton & Gray 2008; Gray & Ancey 2009; Edwards *et al.* 2023). This grows in size, until it occupies the full height of the cell (figure 9*c*,*d*,*e*). The wave then oscillates backwards and forwards in time, eventually approaching a steady state, as shown in figure 9(*e*,*f*) and movies 5. Although the outer margins of the breaking-wave stabilise relatively quickly, the central eye of the wave has oscillations that persist for a very long time. The structure of the steady-state concentration distribution will be solved for explicitly in § 6.

The formation of a series of breaking-size-segregation waves that are aligned with the flow direction is critical for the formation of longitudinal stripes. This is because they allow large particles, which are drawn down to the base of the flow in the downwelling regions, to segregate upwards as soon as they encounter small particles above them. Conversely small particles, which rise to the surface in the upwelling sections, are able to percolate down to the base as soon as they experience large particles beneath them. In this way, both large and small particles can form their own interpenetrating steady-state recirculation loops within each secondary vortex, as will be explicitly shown in § 6.

Figure 10 and movie 6 show a perspective view of the simultaneous time-dependent development of two surface stripes and the internal particle-size distribution in the $(\tilde{y}, \tilde{z})$ plane. The solution is constructed from the time-dependent solution in a single vortex cell (figure 9), by using the reflective symmetry along adjacent vortex cell boundaries. Initially the particles are inversely graded (i.e. large on top of small) so the free surface appears green. Even as the secondary recirculation steepens and breaks the internal interface between the large and small grains to form a breaking-size-segregation wave, the free surface remains green, i.e. large particles are still on the surface (see figure 10*a*,*b*,*c*,*d*). It is only at approximately $\tilde{t} = 6$ non-dimensional time units, that small particles first break onto the free surface in the centre of upwelling regions. The white region then rapidly widens, so that approximately 70 % of the free surface is occupied by small particles (figure 10*e*). Below the free surface, a breaking-size-segregation wave develops, but it takes a very long time to settle down to steady state (figure 10*f*). As a result, the width of the surface bands of large and small particles oscillates subtly in time, which can be seen in movie 6.

https://doi.org/10.1017/jfm.2026.11311 Published online by Cambridge University Press

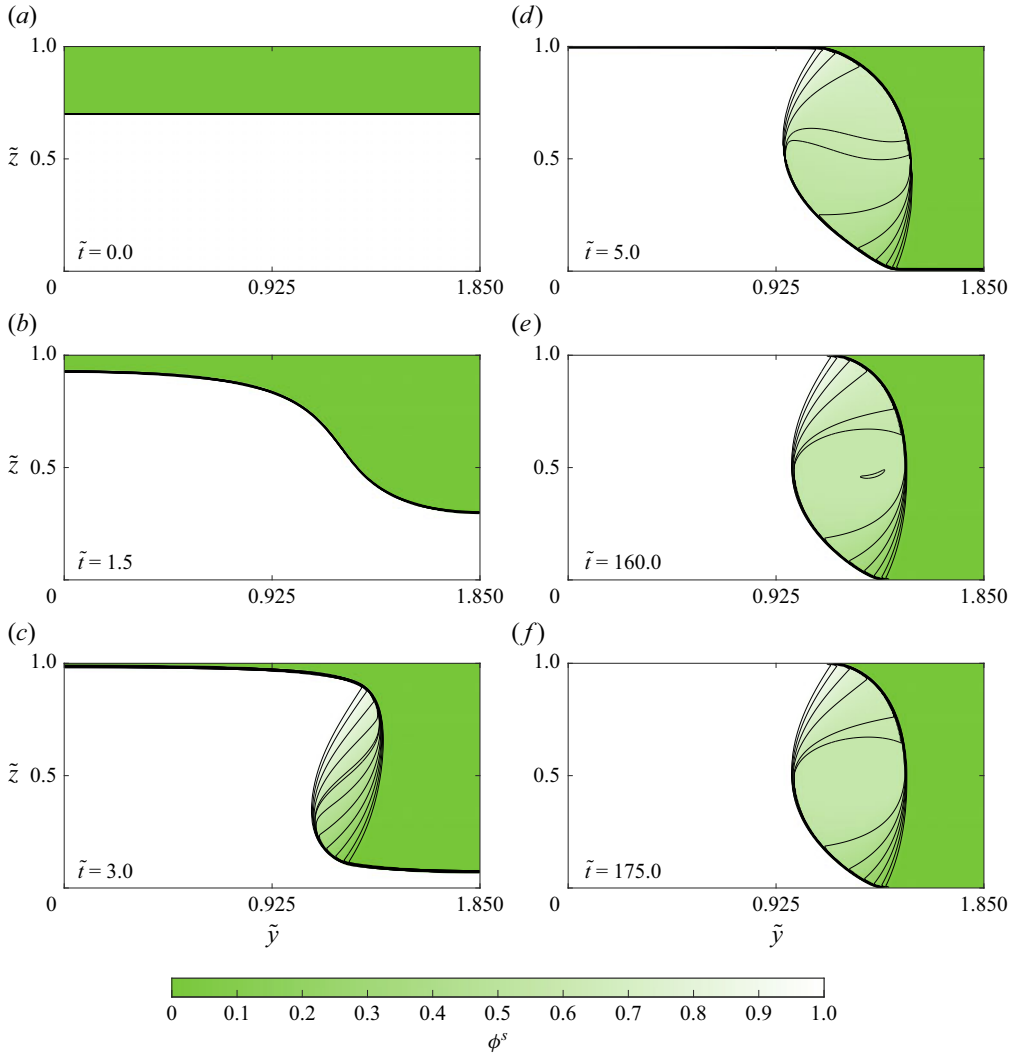


Figure 9. The evolving small-particle concentration ϕ^s at times (*a*) $\tilde{t} = 0$, (*b*) 1.5, (*c*) 3, (*d*) 5, (*e*) 160 and (*f*) steady state $\tilde{t} = 175$ for $\Lambda = 3/2$ and a 30 : 70 mix. The clockwise-rotating secondary vortex is defined in $[0, 1.85] \times [0, 1]$ by the velocities (4.16) and (4.17). The complete time-dependent evolution of the interface is shown in movie 5.

5.3. *The effect of varying* Λ

The effect of varying the ratio Λ of a typical segregation velocity to a typical secondary-recirculation velocity is shown in figure 11. When there is no circulation (i.e. when $\Lambda = \infty$) the steady state corresponds to a inversely graded state with all the large particles separated from the small grains beneath by a concentration shock (figure 11*a*). In the absence of diffusion, any amount of secondary recirculation is sufficient for the horizontal interface between large and small particles to be rotated around and overturn to form a breaking-size-segregation wave, in a similar manner to figures 9 and 10 and movies 5 and 6. If isotropic diffusion is included in the model, then the lateral diffusion may

https://doi.org/10.1017/jfm.2026.11311 Published online by Cambridge University Press

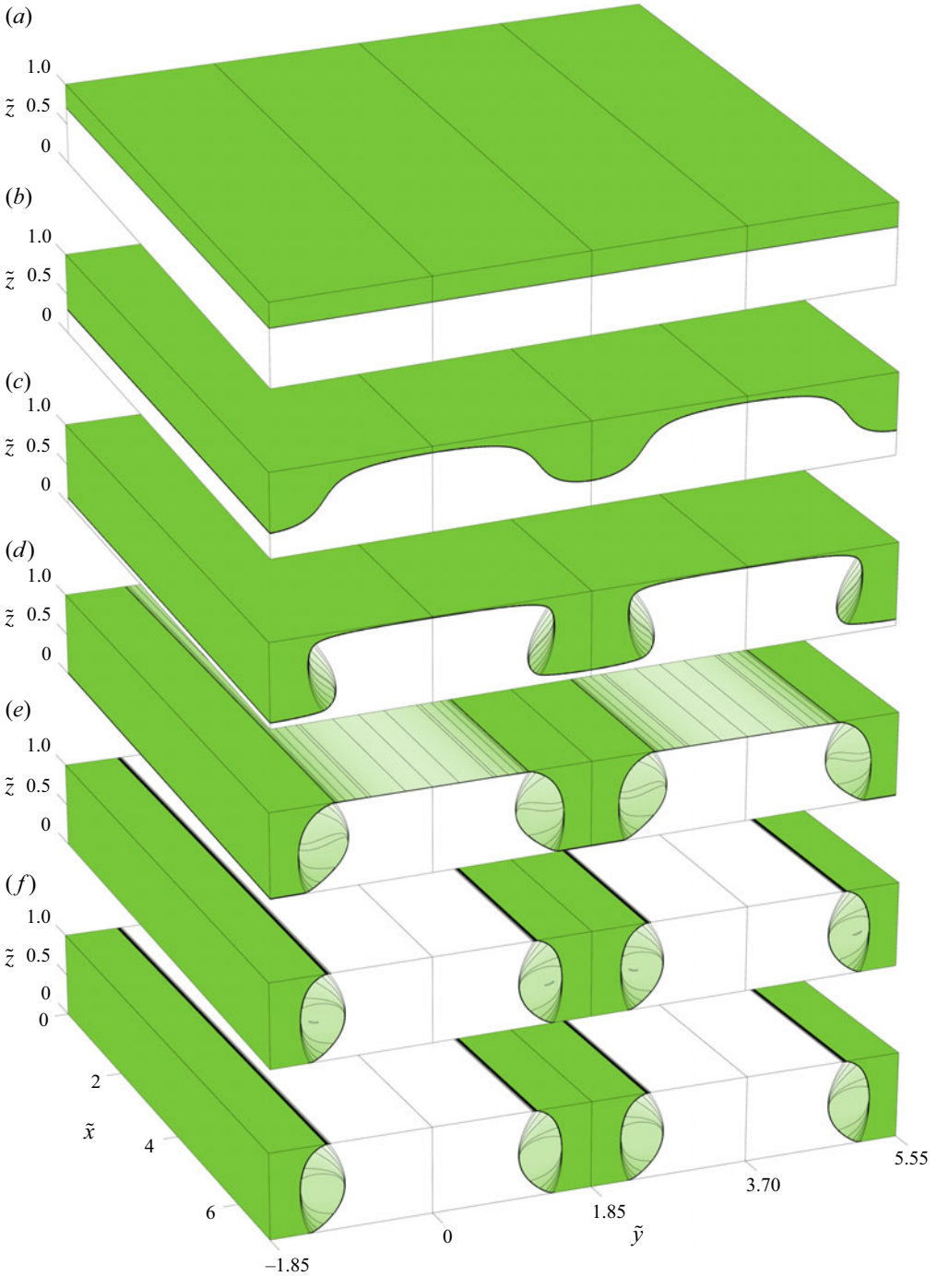


Figure 10. Perspective view of the time-dependent formation of two stripes for $\Lambda = 3/2$ and a 30 : 70 mix that is initially inversely graded. The solution spans four counter-rotating vortex cells. The small-particle concentration $\phi^s(x, y, z, t)$ is shown at non-dimensional times (*a*) $\tilde{t} = 0$, (*b*) 1.5, (*c*) 3, (*d*) 5, (*e*) 160, and approximately at steady state (*f*) $\tilde{t} = 175$. The complete time-dependent evolution is shown in movie 6.

https://doi.org/10.1017/jfm.2026.11311 Published online by Cambridge University Press

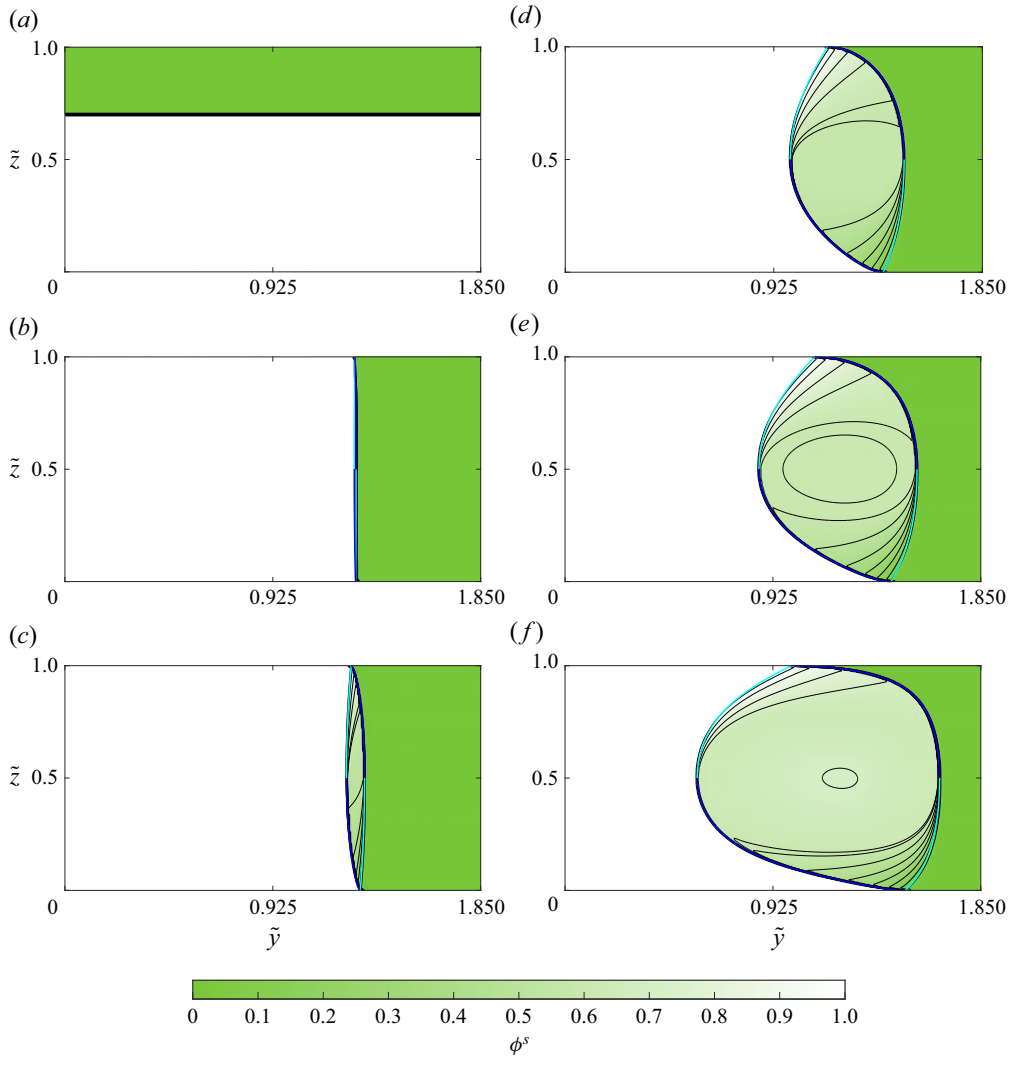


Figure 11. Approximate steady-state numerical solutions for the small-particle concentration ϕ^s for (*a*) $\Lambda = \infty$, (*b*) 100, (*c*) 10, (*d*) 3/2, (*e*) 1 and (*f*) 0.5. The blue and turquoise lines show the steady-state exact solution for the shocks and lead characteristics of the expansion fans, respectively, for comparison. The central eye takes a long time to settle towards steady state. In (*a*) there is no secondary recirculation, and so the interface between small and large particles remains horizontal. In (*b–f*) secondary recirculation is present and a breaking-size-segregation wave forms, which becomes progressively larger as Λ is decreased. Note that the surface concentration is only weakly dependent on the size of the breaking wave.

compete against the steepening of the interface and prevent the formation of breaking-size-segregation waves. This will be investigated in a subsequent paper (Pearse *et al.* submitted).

The focus of this paper is to understand the structure of the breaking-size-segregation waves, and how they are able to recirculate both the large and small particles in the flow to form stable stripes. Figure 11(*b*)–(*f*) shows that when $\Lambda \neq \infty$ steady states are formed with a pure phase of large particles in the downwelling section that is separated from a pure region of small particles in the upwelling section by a breaking-size-segregation wave. As

https://doi.org/10.1017/jfm.2026.11311 Published online by Cambridge University Press

Λ is decreased, the width of the breaking wave increases. Note that in the limit as $\Lambda \to \infty$ from below, the breaking-size-segregation wave essentially collapses onto a vertical shock that lies at $\tilde{y} = 0.7\tilde{W}$ for a 30 : 70 mix (figure 11*b*). This lies perpendicular to the case $\Lambda = \infty$ (no secondary recirculation), i.e. the existence of secondary vortices is a singular perturbation to the problem. Although the width of the breaking-size-segregation waves are sensitively dependent on the value of Λ, their general location is not. In particular, when viewed from above the apparent stripe width is insensitive to the choice of Λ. The fact that the stripes are present across the full parameter space (figure 11*b–f*), apart from when there is no secondary recirculation (figure 11*a*), highlights the robustness of this striped segregation structure.

6. Steady-state exact solution

To understand the behaviour in greater detail it is useful to solve for the steady-state particle-size distribution using the method of characteristics.

6.1. *Quasi-linear form and its transformation to streamfunction coordinates*

At steady state, the non-dimensional incompressibility condition (4.13) can be used to reduce the segregation-advection equation, (4.14), to the quasi-linear form

$$\tilde{v}\frac{\partial \phi^s}{\partial \tilde{y}} + \tilde{w}\frac{\partial \phi^s}{\partial \tilde{z}} + \Lambda(2\phi^s - 1)\frac{\partial \phi^s}{\partial \tilde{z}} = 0. \tag{6.1}$$

Following Gray & Thornton (2005) and Thornton & Gray (2008), it is useful to transform (6.1) into streamfunction coordinates (ξ, ψ) by defining the mapping

$$\xi = \tilde{y}, \qquad \psi = \int_0^{\tilde{z}} \tilde{v}(\tilde{y}, \tilde{z}')\, \mathrm{d}\tilde{z}', \tag{6.2a,b}$$

where ψ, in this case, is now the streamfunction associated with the two-dimensional projected velocity field $\tilde{\boldsymbol{v}} = \tilde{v}\boldsymbol{j} + \tilde{w}\boldsymbol{k}$ in the $(\tilde{y}, \tilde{z})$ plane. In these new coordinates the derivatives transform as

$$\frac{\partial}{\partial \tilde{y}} = \frac{\partial}{\partial \xi} - \tilde{w}\frac{\partial}{\partial \psi}, \qquad \frac{\partial}{\partial \tilde{z}} = \tilde{v}\frac{\partial}{\partial \psi}, \tag{6.3a,b}$$

and hence (6.1) transforms to the reduced quasi-linear form

$$\frac{\partial \phi^s}{\partial \xi} + \Lambda(2\phi^s - 1)\frac{\partial \phi^s}{\partial \psi} = 0, \tag{6.4}$$

provided $\tilde{v} \neq 0$. However, the cross-slope velocity (4.16) is equal to zero in the centre of the domain at $\tilde{z} = 1/2$. The solution is therefore constructed in two transformed domains that lie above and below the no-mean-flow line $\tilde{z} = 1/2$. For the non-dimensional velocity field (4.16)–(4.17) the streamfunction is

$$\psi = \sin\left(\frac{\pi \tilde{y}}{\tilde{W}}\right)(\tilde{z}^2 - \tilde{z}), \tag{6.5}$$

https://doi.org/10.1017/jfm.2026.11311 Published online by Cambridge University Press

which is illustrated in figure 12(*a*). This is quadratic in $\tilde{z}$, so given a mapped position (ξ, ψ) it maps to the physical point $(\tilde{y}, \tilde{z})$ by setting

$$\tilde{y} = \xi, \qquad \tilde{z} = \frac{1}{2}\left(1 \pm \sqrt{1 + \frac{4\psi}{\sin\left(\dfrac{\pi\xi}{\tilde{W}}\right)}}\right), \tag{6.6a,b}$$

where the positive root lies in the upper domain, above $\tilde{z} = 1/2$, and the negative root lies in the lower domain. Note that, on the top, bottom and sides of the secondary vortices $\psi = 0$, while on the $\tilde{z} = 1/2$ line its value is given by

$$\psi = \psi_m(\xi) = -\frac{1}{4}\sin\left(\frac{\pi\xi}{\tilde{W}}\right). \tag{6.7}$$

Since, by definition

$$\frac{\partial\psi}{\partial\tilde{z}} = \tilde{v}, \tag{6.8}$$

the height $\tilde{z} = 1/2$ marks the points where $\partial\psi/\partial\tilde{z} = 0$, and the streamfunction reaches a local maximum, or minimum, dependent on whether the cell is rotating clockwise, or anticlockwise, for a fixed value of ξ. The global maximum and minimum of the streamfunction is

$$\psi_{max/min} = \frac{(-1)^{n+1}}{4}, \quad \text{at} \quad \tilde{y} = \frac{2n+1}{2}\tilde{W}, \quad n = \ldots, -1, 0, 1, 2, \ldots. \tag{6.9}$$

The mapping (6.2) has the advantage that the transformed segregation-advection equation, (6.4), is completely independent of the velocity field, allowing it to be solved in a generic way. The velocity field only re-enters the problem in defining the streamfunction coordinate (6.5) and its return mapping (6.6).

6.2. *Solution by the method of characteristics*

Suppose that λ parameterises the path of a characteristic curve $(\xi(\lambda), \psi(\lambda))$, then the rate of change of the concentration along the characteristic curve

$$\frac{\mathrm{d}\phi^s}{\mathrm{d}\lambda} = \frac{\partial\phi^s}{\partial\xi}\frac{\mathrm{d}\xi}{\mathrm{d}\lambda} + \frac{\partial\phi^s}{\partial\psi}\frac{\mathrm{d}\psi}{\mathrm{d}\lambda}. \tag{6.10}$$

Comparing (6.4) with (6.10) implies that the characteristic equations are

$$\frac{\mathrm{d}\phi^s}{\mathrm{d}\lambda} = 0, \qquad \frac{\mathrm{d}\xi}{\mathrm{d}\lambda} = 1, \qquad \frac{\mathrm{d}\psi}{\mathrm{d}\lambda} = \Lambda(2\phi^s - 1). \tag{6.11a,b,c}$$

Using the chain rule to eliminate λ between equations (6.11*a*) and (6.11*b*), and then solving the resulting ordinary differential equation (ODE), it follows that the concentration is equal to a constant ϕ^s_λ (say) along the characteristic curve λ, i.e.

$$\phi^s = \phi^s_\lambda, \quad \text{on characteristic } \lambda. \tag{6.12}$$

Using this, and the chain rule, equations (6.11*b*,*c*) imply that the shape of the characteristic curve λ is given by solving the ODE

$$\frac{\mathrm{d}\psi}{\mathrm{d}\xi} = \Lambda(2\phi^s_\lambda - 1). \tag{6.13}$$

https://doi.org/10.1017/jfm.2026.11311 Published online by Cambridge University Press

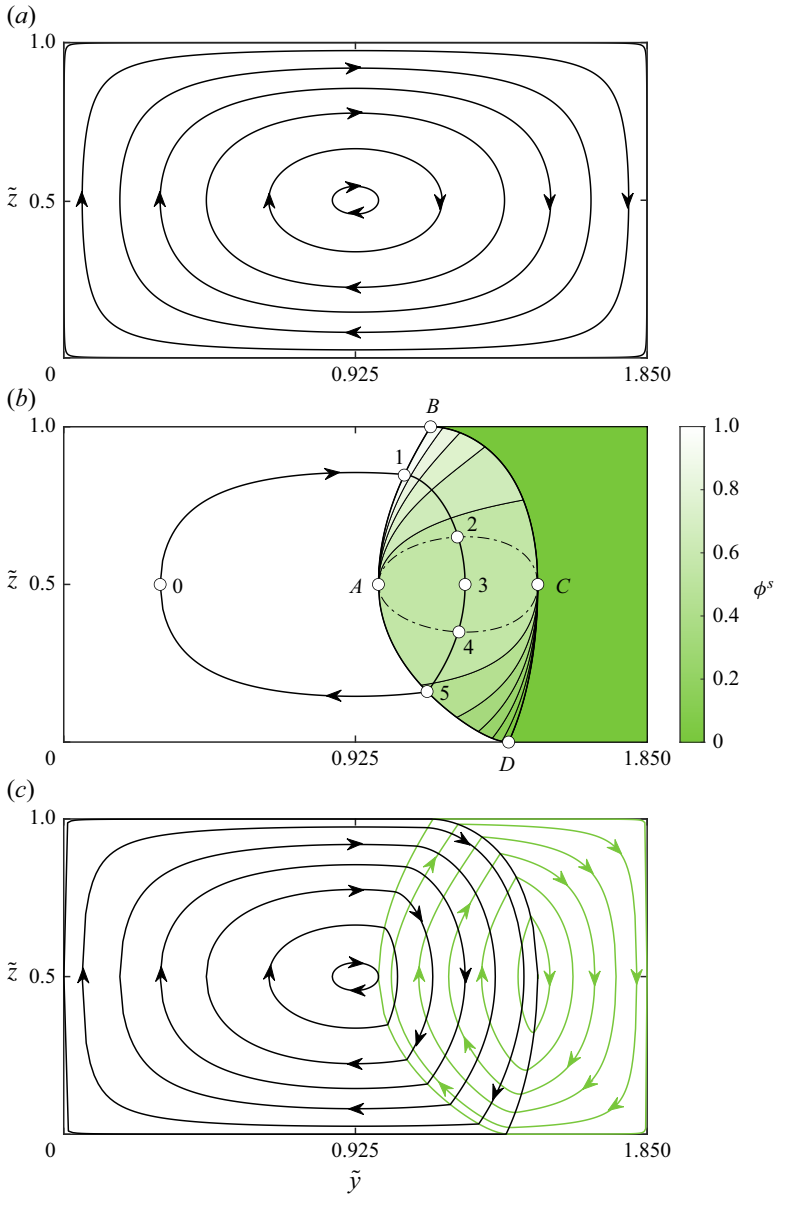


Figure 12. A schematic diagram showing (*a*) the streamfunction coordinates, (*b*) the steady-state breaking-size-segregation wave and (*c*) the large- and small-particle paths for $\Lambda = 3/2$ and a 30 : 70 bidisperse mixture of large and small particles. The exact concentration solution (*b*) consists of two expansion fans, centred at A and C, which intersect the surface and base of the flow at points B and D, respectively. There are two shocks BC and DA, and a central eye of constant concentration that lies between the dot-dashed lines. A single small-particle path is also illustrated in (*b*). It starts in the pure phase of small particles at point 0 on the $\tilde{z} = 1/2$ line and then intersects with 1 the lead characteristic of the top fan, 2 the top eye, 3 the $\tilde{z} = 1/2$ line for the second time, 4 the lower eye, 5 the lower shock and then reconnects at 0 to form a closed loop. (*c*) Shows a series of both small-particle paths (black) and large-particle paths (green). These allow for the simultaneous steady recirculation of both species within a single secondary vortex.

https://doi.org/10.1017/jfm.2026.11311 Published online by Cambridge University Press

Assuming that the characteristic starts at $(\xi, \psi) = (\xi_\lambda, \psi_\lambda)$, then integrating (6.13) shows that the characteristics are straight lines

$$\psi = \psi_\lambda + \Lambda(2\phi_\lambda^s - 1)(\xi - \xi_\lambda), \tag{6.14}$$

in streamfunction coordinates. The method of characteristics allows the solution to be constructed within the smoothly varying parts of the flow. However, the numerically computed steady-state solutions, shown in figure 11, contain two concentration shocks. These have to be solved for using jump conditions (Chadwick 1976; Gray & Thornton 2005; Thornton, Gray & Hogg 2006).

6.3. *Jump conditions across the concentration shocks*

Given that the non-dimensional small-particle segregation-advection equation, (4.14), is in conservative form, the associated jump condition is

$$\left[\!\!\left[\frac{1}{\Lambda}\phi^s\, \tilde{\boldsymbol{v}} \cdot \boldsymbol{n} - \tilde{v}_n \right]\!\!\right] = \left[\!\!\left[\phi^s(1-\phi^s)\boldsymbol{k} \cdot \boldsymbol{n} \right]\!\!\right], \tag{6.15}$$

where $\boldsymbol{n}$ is the two-dimensional unit normal to the shock within the cross-slope plane, the jump bracket $[\![f]\!] = f_+ - f_-$ is the difference of the enclosed quantity on the forward and rearward sides of the discontinuity and $\tilde{v}_n$ is the non-dimensional shock propagation speed. At steady state the shock does not move and $\tilde{v}_n = 0$. For a shock lying at height $\tilde{z} = \tilde{s}(\tilde{y})$, with unit normal $\boldsymbol{n} = (-\mathrm{d}\tilde{s}/\mathrm{d}\tilde{y}, 1)/(1 + (\mathrm{d}\tilde{s}/\mathrm{d}\tilde{y})^2)^{1/2}$, the jump condition therefore reduces to

$$-\tilde{v}\frac{\mathrm{d}\tilde{s}}{\mathrm{d}\tilde{y}} + \tilde{w} = \Lambda(1 - \phi_+^s - \phi_-^s), \quad \text{at} \quad \tilde{z} = \tilde{s}. \tag{6.16}$$

Note, by definition of the streamfunction coordinates (6.2*a*,*b*)

$$\frac{\mathrm{d}}{\mathrm{d}\xi}(\psi(\tilde{s})) = \frac{\mathrm{d}}{\mathrm{d}\tilde{y}}\left(\int_0^{\tilde{s}(\tilde{y})} \tilde{v}(\tilde{y}, \tilde{z}')\, \mathrm{d}\tilde{z}' \right). \tag{6.17}$$

Using Leibniz' rule to exchange the order of differentiation and integration it follows that

$$\frac{\mathrm{d}}{\mathrm{d}\xi}(\psi(\tilde{s})) = \int_0^{\tilde{s}(\tilde{y})} \frac{\mathrm{d}}{\mathrm{d}\tilde{y}}(\tilde{v}(\tilde{y}, \tilde{z}'))\, \mathrm{d}\tilde{z}' + \tilde{v}(\tilde{y}, \tilde{s}(\tilde{y}))\frac{\mathrm{d}\tilde{s}}{\mathrm{d}\tilde{y}}. \tag{6.18}$$

The integral on the right-hand side can be performed directly by substituting the incompressibility condition (4.13) and using the fact that the normal velocity along the base is equal to zero $\tilde{w}(\tilde{y}, 0) = 0$ to obtain

$$\frac{\mathrm{d}}{\mathrm{d}\xi}(\psi(\tilde{s})) = -\tilde{w}(\tilde{y}, \tilde{s}(\tilde{y})) + \tilde{v}(\tilde{y}, \tilde{s}(\tilde{y}))\frac{\mathrm{d}\tilde{s}}{\mathrm{d}\tilde{y}}, \tag{6.19}$$

and hence that in streamfunction coordinates the shock condition (6.16) reduces to

$$\frac{\mathrm{d}}{\mathrm{d}\xi}(\psi(\tilde{s})) = \Lambda(\phi_+^s + \phi_-^s - 1), \quad \text{on} \quad \psi = \psi(\tilde{s}). \tag{6.20}$$

6.4. *Solving for the breaking-size-segregation wave*

The steady-state breaking-size-segregation waves in figure 11 do not move and are aligned with the downslope coordinate. They are therefore perpendicular to the breaking-size-segregation waves found by Thornton & Gray (2008), Gray & Ancey (2009) and Gray & Kokelaar (2010*b*) which travelled downslope at a constant speed. Figure 12(*b*) shows a

https://doi.org/10.1017/jfm.2026.11311 Published online by Cambridge University Press

schematic diagram of the breaking-wave structure in a clockwise rotating cell (figure 8). Unlike earlier breaking-size-segregation waves, the ones that form between the stripes extend through the whole flow depth.

The solution is started at an arbitrary point A along the $\tilde{z} = 1/2$ line as shown in figure 12(*b*). This point has coordinates (ξ_A, ψ_A), where $\psi_A = \psi_m(\xi_A)$ and the function ψ_m, defined in (6.7), determines ψ at an arbitrary point on the $\tilde{z} = 1/2$ line. The solution has an expansion fan centred at (ξ_A, ψ_A), which propagates upwards into the upper half domain. The concentration within the fan is found by solving for ϕ^s in the characteristic (6.14) to give

$$\phi^s = \frac{1}{2}\left(1 + \frac{\psi - \psi_A}{\Lambda(\xi - \xi_A)}\right). \tag{6.21}$$

The lead characteristic AB, on which $\phi^s = 1$, defines the outer boundary of the breaking-size-segregation wave

$$\psi = \psi_A + \Lambda(\xi - \xi_A). \tag{6.22}$$

This outer boundary rises until it intersects with the free surface at point B, which lies at

$$\xi_B = \xi_A - \frac{\psi_A}{\Lambda}, \qquad \psi_B = 0. \tag{6.23a,b}$$

A concentration shock forms along BC. It has large particles on one side ($\phi^s_+ = 0$) and the expansion fan (6.21) on the other. The shock condition (6.20) therefore implies

$$\frac{\mathrm{d}\psi}{\mathrm{d}\xi} = \frac{1}{2}\left(\frac{\psi - \psi_A}{\xi - \xi_A} - \Lambda\right). \tag{6.24}$$

This can be solved, subject to the initial condition that $\psi = \psi_B$ at $\xi = \xi_B$, to give the shape of the upper shock

$$\psi = \psi_A - \Lambda(\xi - \xi_A) + 2\sqrt{-\psi_A \Lambda(\xi - \xi_A)}. \tag{6.25}$$

This shock reaches the $\tilde{z} = 1/2$ line at point C. Its position (ξ_C, ψ_C) can be found by iteratively solving for ξ_C with the equation

$$\psi_C = \psi_m(\xi_C) = \psi_A - \Lambda(\xi_C - \xi_A) + 2\sqrt{-\psi_A \Lambda(\xi_C - \xi_A)}, \tag{6.26}$$

where the function $\psi_m = \psi_m(\xi)$ is defined in (6.7). Here the shock breaks to form another expansion fan that propagates downwards into the lower domain. The fan is centred at (ξ_C, ψ_C), and the concentration within it is given by

$$\phi^s = \frac{1}{2}\left(1 + \frac{\psi_C - \psi}{\Lambda(\xi_C - \xi)}\right). \tag{6.27}$$

The boundary between the breaking-size-segregation wave and the region of large particles is given by the $\phi^s = 0$ characteristic

$$\psi = \psi_C + \Lambda(\xi_C - \xi). \tag{6.28}$$

This reaches the base of the flow at

$$\xi_D = \xi_C + \frac{\psi_C}{\Lambda}, \qquad \psi_D = 0, \tag{6.29a,b}$$

https://doi.org/10.1017/jfm.2026.11311 Published online by Cambridge University Press

where a shock DA is generated between the small particles and the lower expansion fan (6.27). The shock condition (6.20) implies that

$$\frac{\mathrm{d}\psi}{\mathrm{d}\xi} = \frac{1}{2}\left(\Lambda + \frac{\psi_C - \psi}{\xi_C - \xi}\right), \tag{6.30}$$

which can be solved, subject to the condition that $\psi = \psi_D$ at $\xi = \xi_D$, to give the shape of the lower shock

$$\psi = \psi_C - \Lambda(\xi_C - \xi) + 2\sqrt{-\psi_C \Lambda(\xi_C - \xi)}. \tag{6.31}$$

In order for the breaking wave to form a closed structure, the lower shock (6.31) must intersect the original point (ξ_A, ψ_A) as it breaks to form the upper expansion fan (6.21).

As in the case of the breaking wave constructed by Gray & Ancey (2009), the solution has a central eye of constant concentration

$$\phi^s_{eye} = \frac{1}{2}\left(1 + \frac{\psi_C - \psi_A}{\Lambda(\xi_C - \xi_A)}\right), \tag{6.32}$$

which is bounded above and below by the characteristics

$$\psi^{upper}_{eye} = \psi_A + (2\phi^s_{eye} - 1)\Lambda(\xi - \xi_A), \tag{6.33}$$

$$\psi^{\mathrm{lower}}_{eye} = \psi_C - (2\phi^s_{eye} - 1)\Lambda(\xi_C - \xi). \tag{6.34}$$

These characteristics are shown in figure 12(*b*), and emanate out of, and connect between, the fans centred at (ξ_A, ψ_A) and (ξ_C, ψ_C), i.e. they both imply

$$\psi_C = \psi_A + (2\phi^s_{eye} - 1)\Lambda(\xi_C - \xi_A), \tag{6.35}$$

consistent with (6.32). In particular, substituting for ψ_C in (6.34) from (6.35) implies that the boundary of the lower eye can equivalently be expressed as

$$\psi^{\mathrm{lower}}_{eye} = \psi_A + (2\phi^s_{eye} - 1)\Lambda(\xi - \xi_A), \tag{6.36}$$

which in streamfunction coordinates is the same as the boundary (6.33) for the upper eye. This fact will be useful later in solving for the particle paths, although it should be stressed that the upper and lower boundaries of the eye lie in the upper and lower streamfunction domains, respectively, so (6.33) and (6.36) represent different physical boundaries. Note that the solution in the upper domain (6.21)–(6.23), (6.25) and (6.33) can be transformed to the solution in the lower domain (6.27)–(6.29), (6.31) and (6.34) by the mapping

$$\xi \mapsto -\xi, \quad \psi \mapsto \psi, \quad \phi^s \mapsto 1 - \phi^s, \quad A \mapsto C, \quad B \mapsto D, \quad C \mapsto A. \tag{6.37a–f}$$

This will be useful in Appendices A and B for tracking the large- and small-particle paths (figure 12*b*,*c*). The combination of the two expansion fans, two shocks and the central eye of constant concentration, forms a steady-state breaking-size-segregation wave (Thornton & Gray 2008; Gray & Ancey 2009; Johnson *et al.* 2012; Edwards *et al.* 2023). In contrast to previous solutions, the wave extends through the full depth of the flow, is spatially uniform in the downslope direction and connects the pure region of large grains to the pure region of fines, allowing stripes to be seen at the surface (as shown in figures 7 and 10). A comparison between the computed steady-state and the exact solution for a range of Λ is shown in figure 11. The position of the lead expansions, the shocks and hence the overall size of the steady-state breaking-size-segregation waves is in almost exact agreement with the computed solutions. However, the central eye of constant concentration takes a very long time to equilibrate, and this aspect of the numerical solution has not yet reached steady state.

https://doi.org/10.1017/jfm.2026.11311 Published online by Cambridge University Press

7. Particle paths

The breaking-size-segregation waves separate the pure regions of large and small particles in the stripes. Crucially, they allow large and small particles to be recirculated within a single secondary vortex. It is of interest to understand exactly how this is achieved.

7.1. *Three-dimensional bulk, small- and large-particle paths*

The particle paths in the bulk flow field, and of the large and small grains, are given by solving the differential equations

$$\frac{\mathrm{d}\tilde{x}}{\mathrm{d}\tilde{t}} = \tilde{u}, \qquad \frac{\mathrm{d}\tilde{y}}{\mathrm{d}\tilde{t}} = \tilde{v}, \qquad \frac{\mathrm{d}\tilde{z}}{\mathrm{d}\tilde{t}} = \tilde{w}, \qquad \frac{\mathrm{d}\tilde{z}^l}{\mathrm{d}\tilde{t}} = \tilde{w}^l, \qquad \frac{\mathrm{d}\tilde{z}^s}{\mathrm{d}\tilde{t}} = \tilde{w}^s, \tag{7.1a–e}$$

where the non-dimensional large- and small-particle velocities

$$\tilde{w}^l = \tilde{w} + \Lambda\phi^s, \qquad \text{and} \qquad \tilde{w}^s = \tilde{w} - \Lambda(1-\phi^s), \tag{7.2a,b}$$

follow from (4.2), (4.3) and the scalings (4.12) (Gray & Thornton 2005; Thornton *et al.* 2006; Gray & Ancey 2009). Under the assumption of spatial uniformity in the downslope direction, the non-dimensional downslope velocity uncouples from the segregation problem, but $\tilde{u}$ is needed to solve for the particle paths. In (7.1) the downslope velocity and downslope length are assumed to scale as

$$u = u^*\tilde{u}, \qquad x = \left(\frac{u^*H}{q}\right)\tilde{x}, \tag{7.3a,b}$$

where, recall from (3.1), u^* is a typical downslope surface velocity magnitude. Since the downslope velocity is typically a lot larger than the segregation velocity ($u^* \gg q$), it follows that a typical downslope length scale $L = u^*H/q$ is much larger than H. Using the scalings (4.12) and (7.3) it follows that the non-dimensional downslope velocity is

$$\tilde{u} = 1 - (1-\tilde{z})^{\frac{3}{2}}. \tag{7.4}$$

Equations (7.1), (7.2) and (7.4) form three sets of coupled ODEs that can be solved numerically for the bulk, small- and large-particle paths assuming the exact small-particle concentration solution derived in § 6.4.

7.2. *The case of a 30 : 70 mix*

Figure 13 shows a three-dimensional perspective view of the solution surfaces that are generated for a 30 : 70 mix with $\Lambda = 3/2$, by initially releasing a series of particles along the $\tilde{x} = 0$, $\tilde{z} = 1/2$ (orange) line and integrating their trajectories up until $\tilde{t} = 20$ to find their final positions (red line). Individual paths are shown by the magenta, yellow, cyan, white and green lines. The solution surfaces are complex even for the prescribed bulk flow field (figure 13*a*). In it, the magenta line starts closest to the cell boundary and describes a looping path that takes it through both high and low downslope velocity regions, near the surface and base of the flow, respectively. Particles on the magenta line therefore make most of their progress downslope when they are near the surface of the flow. In contrast, the green particle path starts near the centre of the vortex cell close to $\tilde{y} = \tilde{W}/2$, and describes small oscillations around the centre of the vortex moving at almost constant speed downslope. After twenty non-dimensional time units the green trajectory has moved slightly further downslope than the magenta one. Intermediate trajectories describe loops of increasing amplitude the further away they start from the centre of the

https://doi.org/10.1017/jfm.2026.11311 Published online by Cambridge University Press

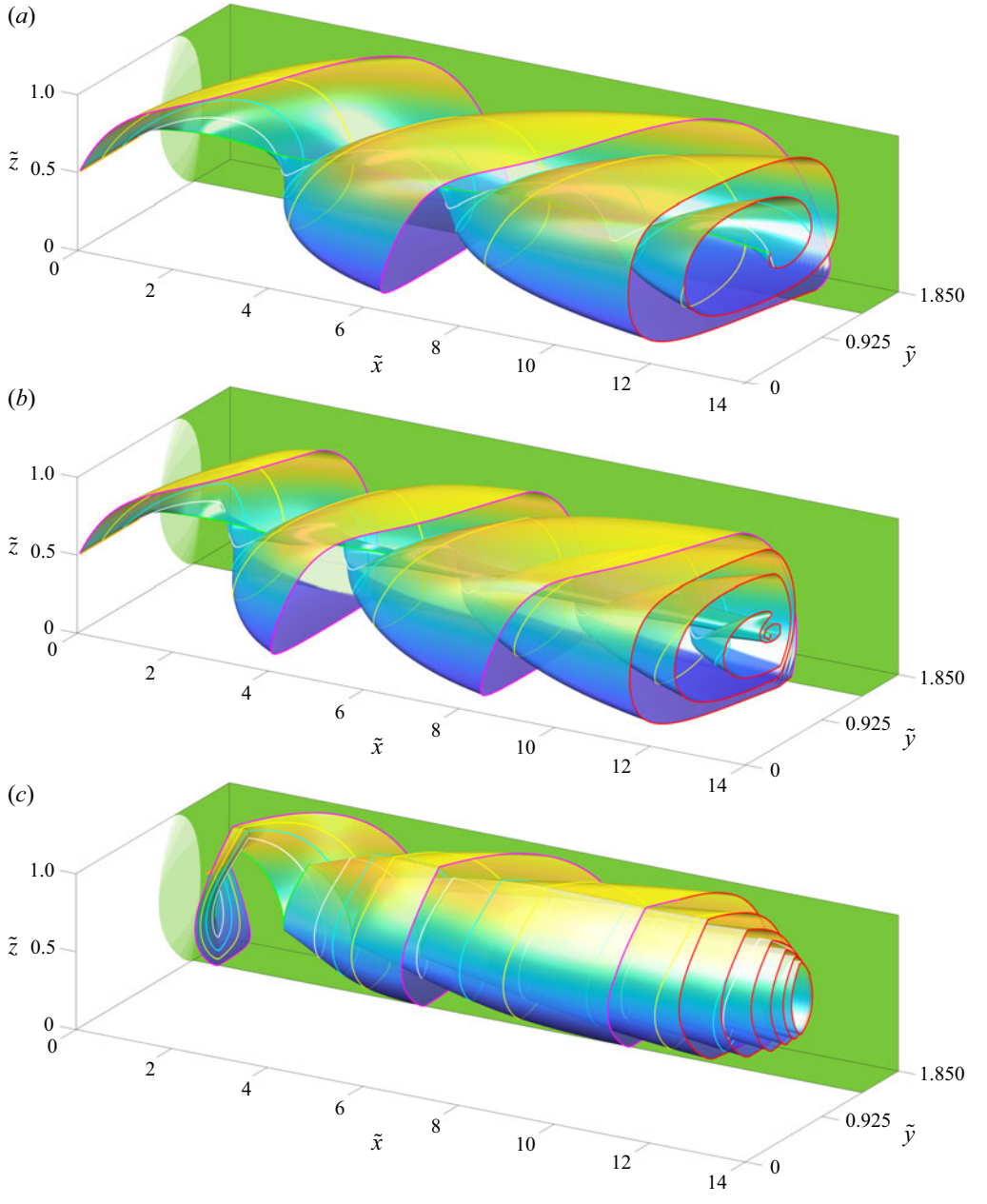


Figure 13. Three-dimensional surfaces formed by the trajectories of (*a*) bulk, (*b*) small and (*c*) large particles that are released in a single clockwise rotating secondary vortex with $\Lambda = 3/2$. The trajectories assume a steady-state particle-size distribution for a 30 : 70 mix of large and small particles (shown on the base, side and rear walls). Particles that are released along the orange line (along $\tilde{x} = 0$, $\tilde{z} = 1/2$) are transported downstream and by $\tilde{t} = 20$ non-dimensional times units lie along the red line. Individual trajectories are shown with the magenta, yellow, cyan, white and green lines. At $\tilde{t} = 0$ the magenta line is close to the exterior of the cell and the green line is close to (*a*) $\tilde{W}/2$, (*b*) $\tilde{y}_A$ and (*c*) $\tilde{y}_C$. The surface colour indicates the flow depth. A Bagnold velocity (7.4) is assumed in the $\tilde{x}$ direction, so that grains that are higher in the flow move faster down slope. Movies 7, 8 and 9 show animated flybys of each of the surfaces.

https://doi.org/10.1017/jfm.2026.11311 Published online by Cambridge University Press

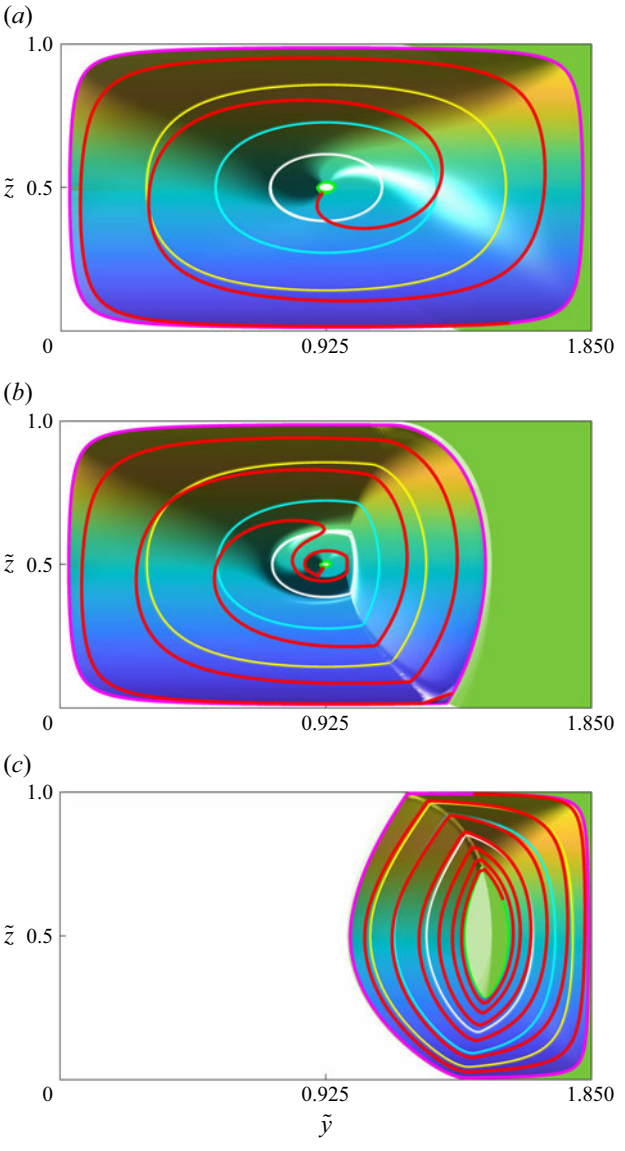


Figure 14. View down the secondary-vortex axis showing the (*a*) bulk, (*b*) small- and (*c*) large-particle paths in figure 13 for $\Lambda = 3/2$ and a 30 : 70 mix of large and small particles. Note that, when projected on to the $(\tilde{y}, \tilde{z})$ plane, the looping magenta, yellow, cyan, white and green particle paths form closed loops. In addition, particles that were initially released from various positions along the $\tilde{x} = 0$, $\tilde{z} = 1/2$ line, end up on the spiralling red line after $\tilde{t} = 20$ non-dimensional times units.

vortex $(\tilde{W}/2, 1/2)$, and the greatest downstream motion is achieved along one of these intermediate paths. When viewed down the axis of the vortex (figure 14*a*) the bulk particle paths form closed loops when they are projected onto the $(\tilde{y}, \tilde{z})$ plane. In Appendix A it is shown that these bulk particle paths correspond to isolines of the streamfunction. By $\tilde{t} = 20$ non-dimensional time units the bulk particles that started along the $\tilde{x} = 0$, $\tilde{z} = 1/2$ line, end up along the spiralling red line, and the green path has performed nearly four oscillations, whilst the magenta path has only performed approximately 1.75

https://doi.org/10.1017/jfm.2026.11311 Published online by Cambridge University Press

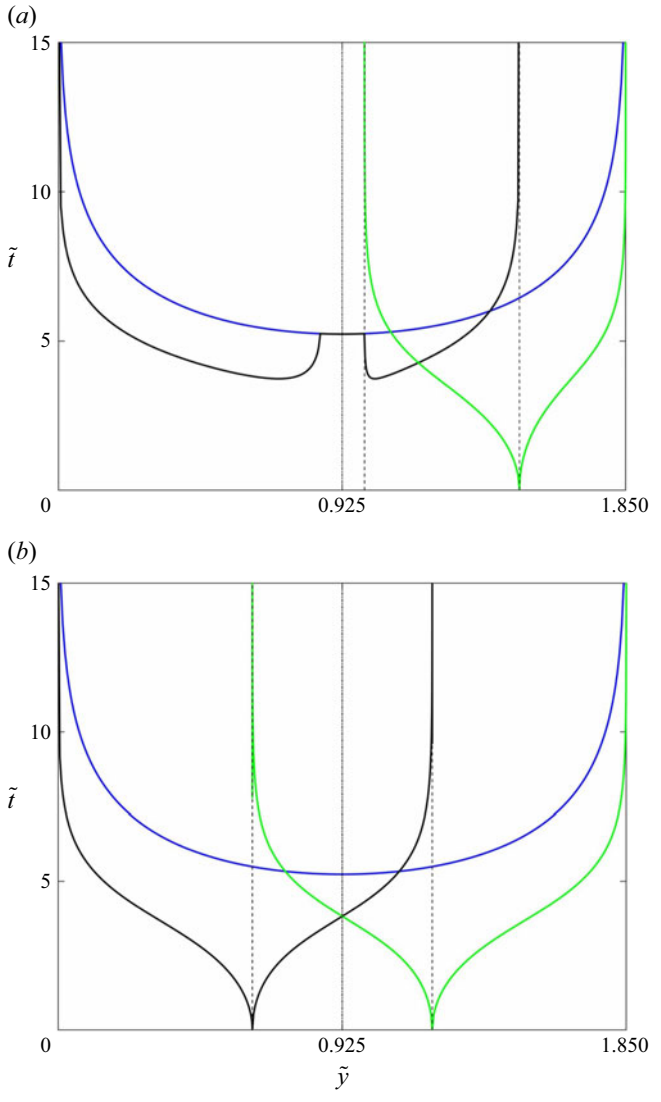


Figure 15. The time taken to complete a loop of the bulk (blue line), small (black line) and large (green line) projected particle paths at different starting positions $\tilde{y}$ along the $\tilde{z} = 1/2$ line for (*a*) a 30 : 70 and (*b*) a 50 : 50 mix of large and small particles. The dashed lines indicate the positions of $\tilde{y}_A$ and $\tilde{y}_C$ where there are zeros and singularities. The dot-dash line marks the centre of the cell.

oscillations. The difference determines the number of loops in the red spiral. The time taken to complete a loop of a projected bulk particle path as a function of the starting position $\tilde{y}$ along the $\tilde{z} = 1/2$ line is shown in figure 15. There are two singularities at $\tilde{y} = 0$ and $\tilde{y} = \tilde{W} = 1.85$, which correspond to the exterior boundary of the cell. Particles on the $\psi = 0$ path therefore take an infinite time to complete a circuit, which is because both $\tilde{v}$ and $\tilde{w}$ tend to zero in the four corners of the cell. The minimum time to complete a circuit is achieved in the centre of the cell at $\tilde{y} = \tilde{W}/2$.

https://doi.org/10.1017/jfm.2026.11311 Published online by Cambridge University Press

Figure 13(*b*) shows a similar surface swept out for a series of small-particle paths that initially start in the pure small phase on the $\tilde{x} = 0, \tilde{z} = 1/2$ line. The magenta line is again close to the cell boundary, while this time the green path is close to the point $\tilde{y}_A$. Looking down the axis of the breaking-size-segregation wave (figure 14*b*) the green trajectory stays entirely within the region of small particles, so it rotates at the same speed as the bulk flow. Conversely, the white, cyan, yellow and magenta paths all pass through the breaking-size-segregation wave, and form closed loops of increasing amplitude in the projected plane. Exact solutions for the projected small-particle paths, illustrated in figure 12(*b*,*c*), are given in Appendix A. Figure 15(*a*) shows the time taken for small particles to perform a loop of the projected particle paths. For a 30 : 70 mix there is a region around the centre of the cell $\tilde{y} \in [\tilde{W} - \tilde{y}_A, \tilde{y}_A]$, where the small particles perform loops entirely within the small-particle region. In this region the time taken for a small particle to complete a loop is the same as for the bulk flow. Outside this region small particles pass through the both the small-particle region and the breaking-size-segregation wave, i.e. for $\tilde{y} \in [0, \tilde{W} - \tilde{y}_A] \cup [\tilde{y}_A, \tilde{y}_C]$. In the limit as $\tilde{y} \to 0$ or $\tilde{y} \to \tilde{y}_C$ the time taken to do a loop tends to infinity. This is again because the path lies on the outer boundary $\psi = 0$ for at least some of the time, where both the cross slope and normal velocity components tend to zero in the cell corners. For intermediate starting positions just outside the central core there is a significant speed up in the time that it takes to do a loop, which is associated with the rapid percolation of the small particles through the breaking-size-segregation wave. Viewed up the vortex axis, the final small-particle positions initially appear to spiral outwards in a clockwise sense, before switching direction to spiral outwards in an anticlockwise sense (figures 13*b* and 14*b*). As a result particles perform more rotations as they are swept downslope than the bulk flow (figures 13*a* and 14*a*).

The circuits performed by the large particles are dramatically different to the bulk and small particles as shown in figures 13(*c*) and 14(*c*). This is because, as well as there being singularities at $\tilde{y} = \tilde{y}_A$ and $\tilde{y} = \tilde{W}$, the time taken to perform a circuit tends to zero as $\tilde{y} \to \tilde{y}_C$ (figure 15*a*). The surface swept out by the initial line of particles therefore wraps around itself very fast as one approaches $\tilde{y}_C$, and the three-dimensional perspective view in figure 13(*c*) and movie 9 has the appearance of a filo pastry. This switch in behaviour is due to the existence of a central core of small particles that do not enter the breaking-size-segregation wave, and therefore forces the small particles to spend a considerable amount of time in the pure phase of small particles. The large particles near $\tilde{y} = \tilde{y}_C$, on the other hand, only have to travel a short distance through the pure large phase before being re-entrained into the breaking-size-segregation wave. In some sense this is similar to the mixing of differently coloured particles in a rotating drum, which also switches behaviour dependent on the existence, or not, of a central slowly rotating core (Gray 2001).

7.3. *The case of a 50 : 50 mix*

The case of a 50 : 50 mix of large and small particles is interesting because there is neither a slowly rotating core of pure large or pure small particles. The time taken for large particles to perform circuits is broadly similar to the 30 : 70 case, with singularities at $\tilde{y} = \tilde{y}_A$ and $\tilde{y} = \tilde{W}$, and a zero at $\tilde{y} = \tilde{y}_C$. However, in the 50 : 50 case, the small particles now have a similar structure to the large particles, with singularities at $\tilde{y} = 0$ and $\tilde{y}_C$, and a zero at $\tilde{y} = \tilde{y}_A$ as shown in figure 15(*b*). The existence of the two zeros now implies that the small-particle paths wrap tightly around $\tilde{y}_A$, while the large-particle paths wrap tightly around $\tilde{y}_C$ as before. As a result the three-dimensional perspective view of the large- and

https://doi.org/10.1017/jfm.2026.11311 Published online by Cambridge University Press

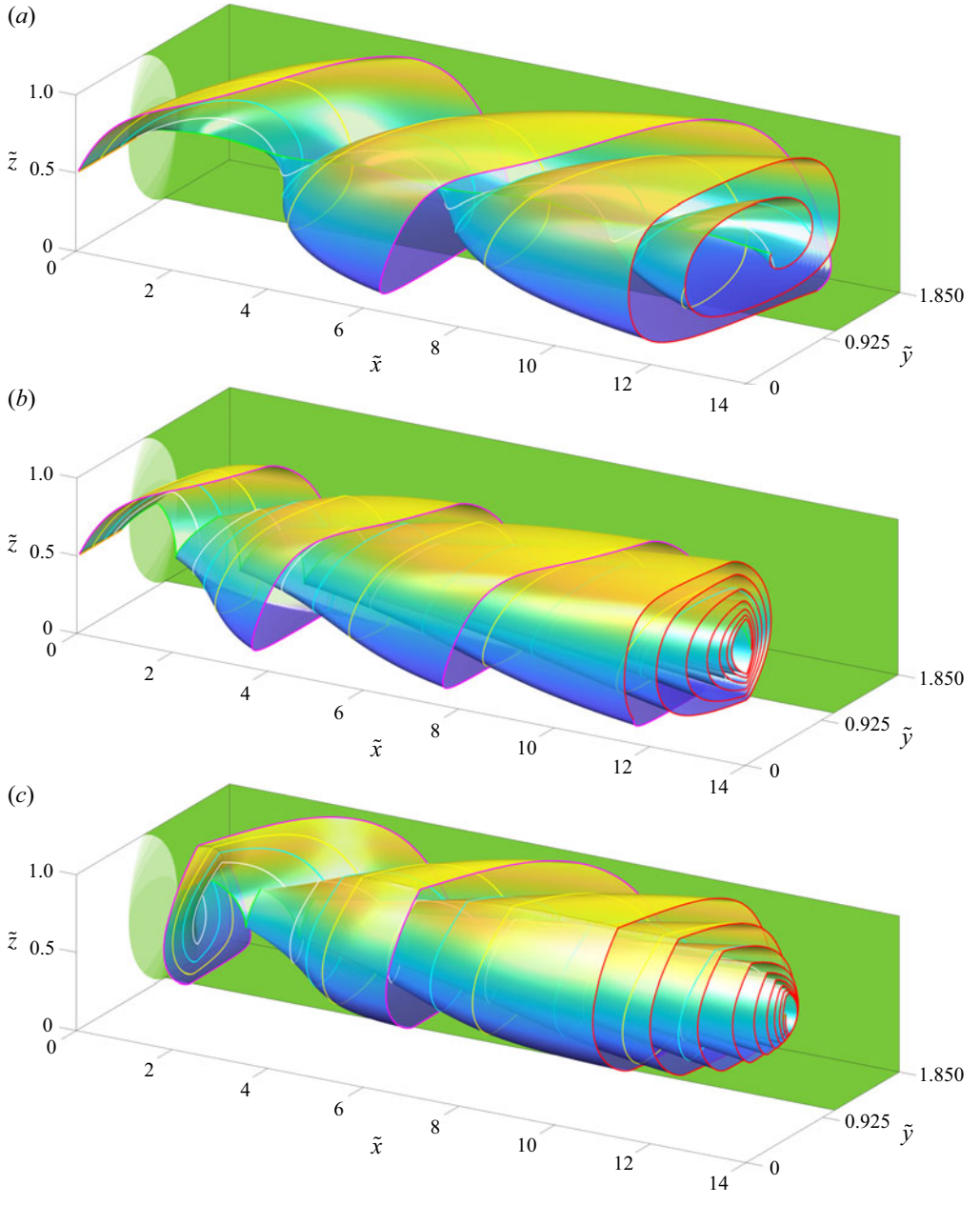


Figure 16. Three-dimensional surfaces formed by the trajectories of (*a*) bulk, (*b*) small and (*c*) large particles that are released in a single clockwise rotating secondary vortex with $\Lambda = 3/2$. The trajectories assume a steady-state particle-size distribution for a 50 : 50 mix of large and small particles (shown on the base, side and rear walls). Particles that are released along the orange line (along $\tilde{x} = 0$, $\tilde{z} = 1/2$) are transported downstream and by $\tilde{t} = 20$ non-dimensional times units lie along the red line. Individual trajectories are shown with the magenta, yellow, cyan, white and green lines. At $\tilde{t} = 0$ the magenta line is close to the exterior of the cell and the green line is close to (*a*) $\tilde{W}/2$, (*b*) $\tilde{y}_A$ and (*c*) $\tilde{y}_C$. The surface colour indicates the flow depth. A Bagnold velocity (7.4) is assumed in the $\tilde{x}$ direction, so that grains that are higher in the flow move faster down slope. Movies 10, 11 and 12 show animated flybys of each of the surfaces.

https://doi.org/10.1017/jfm.2026.11311 Published online by Cambridge University Press

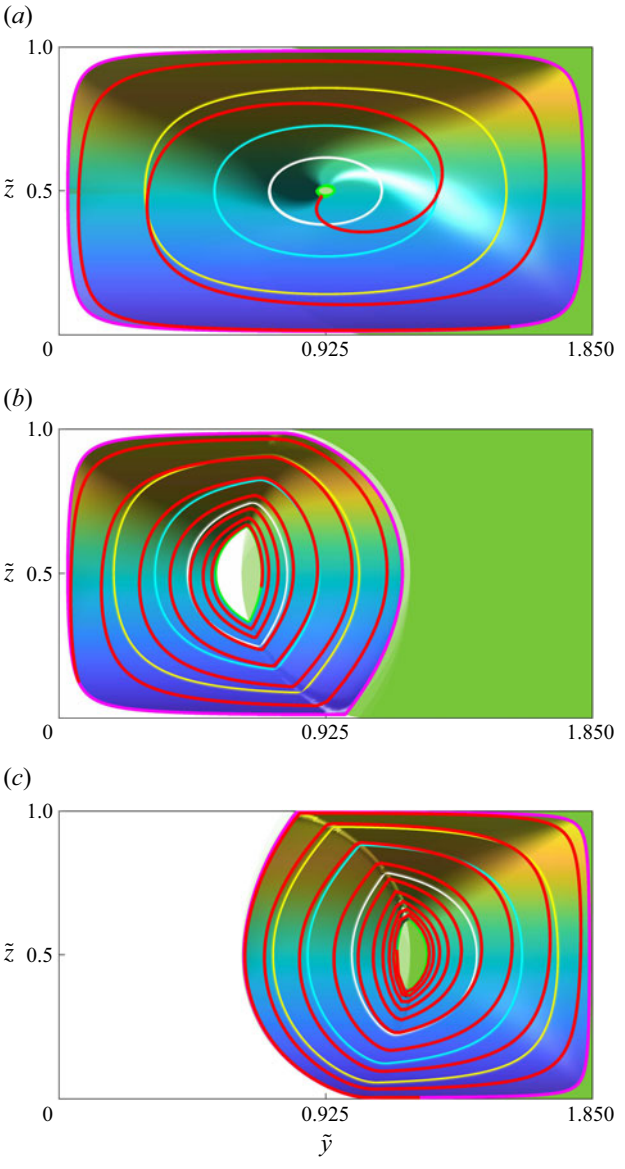


Figure 17. View down the secondary-vortex axis showing the (*a*) bulk, (*b*) small- and (*c*) large-particle paths in figure 16 for $\Lambda = 3/2$ and a 50 : 50 mix of large and small particles. Note that, when projected on to the $(\tilde{y}, \tilde{z})$ plane, the looping magenta, yellow, cyan, white and green particle paths form closed loops. In addition, particles that were initially released from various positions along the $\tilde{x} = 0$, $\tilde{z} = 1/2$ line, end up on the spiralling red line after $\tilde{t} = 20$ non-dimensional times units.

small-particle paths both have the appearance of filo pastries as shown in figures 16(*b*,*c*) and 17(*b*,*c*) as well as movies 11 and 12.

8. Conclusions

This paper shows that particle-size-segregated longitudinal stripes form when a bidisperse mixture of grains avalanches rapidly down a slope (see figures 1–6). On a curved chute

https://doi.org/10.1017/jfm.2026.11311 Published online by Cambridge University Press

the stripes can be preserved in the deposit, and extend all the way through the flow depth (figure 3). Qualitatively the experimental deposits in figures 1–4 look very similar to the long run-out Sherman landslide deposits illustrated in figure 4 of Shreve (1966) and figure 6 of Post (1967), which also have compositional differences between the flow bands. In § 3, a conceptual model is developed that assumes that the stripes form due to a combination of conventional gravity-shear-driven particle-size segregation (e.g. Gray 2018; Trewhela *et al.* 2021) and the rotational overturning generated by secondary vortices that are aligned with the direction of motion. The root cause of the secondary vortices is not fully clear, but it is likely that the flow is in the rapid dense regime observed in monodisperse flows by Börzsönyi *et al.* (2009). The secondary motion is probably driven by dilatation, aided perhaps by second normal stress differences (Gadal *et al.* 2026), but there is currently no continuum theory that is able to quantitatively model such flows. This paper therefore assumes the existence of secondary vortices and solves the associated particle-size segregation problem.

In § 5 the segregation-advection equation, (4.14), is solved numerically in a single secondary vortex in the $(\tilde{y}, \tilde{z})$-plane to show how an inversely graded interface (with large particles above small particles) is rotated around to form a breaking-size-segregation wave. Large particles are concentrated in the downwelling part of the vortex and segregate upwards through the breaking wave, while small particles concentrate in the upwelling section and percolate down through the wave. In this way, two interpenetrating co-rotating sub-vortices are formed that recirculate the large and small grains. Pure phases of large and small particles are therefore able to develop, which extend right the way through the flow depth and remain separated in the cross-slope direction by the breaking wave (see figure 9 and movie 5). These solutions assume uniformity in the downslope x-direction. The breaking waves are therefore three-dimensional structures that align with the dominant downslope motion. To aid understanding, the symmetry of the problem is used to extend the numerical solution to four counter-rotating vortices and show how the structure in the $(\tilde{y}, \tilde{z})$-plane manifests itself on the free surface in a three-dimensional perspective view illustrated in figure 10 and shown in movie 6. Each stripe is formed from adjacent bands of large and small particles that are oriented in the downslope direction. Measured from centre to centre of each large-rich band, a single stripe consists of two counter-rotating vortices as illustrated in the schematic diagram in figure 7.

Although the model is not able to explain the root cause of secondary vortices, it does show that conventional segregation models (e.g. Gray 2018) are able to capture all the phenomenology of the segregation behaviour provided a series of counter-rotating secondary vortices are assumed to exist. It is therefore not necessary to assume some form of lateral segregation that dominates over conventional gravity-shear-driven segregation. Diffusion is not currently included in the model, but it is the next logical extension of the theory, and is the subject of a follow-up paper (Pearse *et al.* submitted). In particular, this shows that lateral diffusion can compete against the vortical overturning and stabilise the interface between large and small particles. In principle, it is therefore still possible to have an inversely graded particle-size distribution even in the presence of secondary vortices.

The experiments in § 2 show that the formation of a longitudinally striped segregation pattern is a sensitive litmus test for the existence of secondary vortices. This secondary recirculation might otherwise go unnoticed. Indeed, if the experiments were performed with a monodisperse material (instead of a differentially coloured bidisperse one) one might never know that a complex secondary flow had developed at all, as the surface bumps that are generated in the deposit are very subtle. Many other apparently mundane granular flows may therefore have secondary flow instabilities. Indeed, the works of Forterre & Pouliquen (2002), Börzsönyi *et al.* (2009), Brodu *et al.* (2013, 2015) and

https://doi.org/10.1017/jfm.2026.11311 Published online by Cambridge University Press

Heyman *et al.* (2017*a*) suggest that unidirectional flows are rare, occurring only for very low inclination thin flows. The existence of secondary recirculation points to deficiencies in our understanding of the rheology of dry granular flows that may yet prove important to understand. In particular, it may provide a partial explanation of longitudinal ridges and flow bands that are frequently observed in the deposits of rapid geophysical mass flows on Earth and other celestial bodies (Shreve 1966; Post 1967; McSaveney 1978; Dufresne & Davies 2009; Magnarini *et al.* 2019; Magarini *et al.* 2021; Magnarini *et al.* 2024).

This paper focusses on the formation of stripes in a bidisperse mixture of grains of the same intrinsic density. However, D'Ortona & Thomas (2020) and D'Ortona *et al.* (2025) have shown that mixtures of large-dense and small-light particles, can develop secondary vortices by a self-induced Raleigh–Taylor-like instability. Since the theory for particle-size and -density segregation is very similar to that of particle-size segregation (Gray & Ancey 2015; Gray 2018), the solutions developed in this paper may find application to this problem. In particular, it may be feasible to include composition-dependent density differences in bi-disperse granular continuum models in a similar manner to the way particle-size differences were included in Barker *et al.* (2021) and Maguire *et al.* (2024). This would open-up the possibility of developing fully coupled theories to capture the segregation-induced secondary recirculation in mixtures of particles of differing size and density.

Supplementary movies. Supplementary movies are available at https://doi.org/10.1017/jfm.2026.11311.

Acknowledgements. We wish to acknowledge preliminary experiments by Dr A. Russell that inspired this paper.

Funding. A.P.P. was supported by an Engineering and Physical Sciences Research Council (EPSRC) Doctoral Training Award. C.G.J. and J.M.N.T.G. were supported by Natural Environment Research Council (NERC) grants NE/X00029X/1 and NE/X013936/1. J.M.N.T.G. was also supported by a Royal Society Wolfson Research Merit Award (WM150058) and an EPSRC Established Career Fellowship (EP/M022447/1).

Declaration of interests. The authors report no conflicts of interest.

Data availability statement. All research data supporting this publication are directly available within this publication.

Appendix A. Bulk and small-particle paths in the projected plane

Since the velocities are independent of time, and the large- and small-particle concentrations are independent of $\tilde{x}$, the system uncouples, allowing the particle paths to be solved for in the projected plane $(\tilde{y}, \tilde{z})$. Using (7.1*b*) to eliminate $\tilde{t}$, it follows that the projected particle-paths of the bulk flow field and the large and small particles satisfy

$$\tilde{v}\frac{\mathrm{d}\tilde{z}}{\mathrm{d}\tilde{y}} - \tilde{w} = 0, \qquad \tilde{v}\frac{\mathrm{d}\tilde{z}^l}{\mathrm{d}\tilde{y}} - \tilde{w} = \Lambda\phi^s, \qquad \tilde{v}\frac{\mathrm{d}\tilde{z}^s}{\mathrm{d}\tilde{y}} - \tilde{w} = -\Lambda(1-\phi^s), \qquad \text{(A1}a\text{–}c\text{)}$$

respectively. These can be transformed to streamfunction coordinates, by using (6.19), to give the bulk, as well as large- and small-particle, projected path equations

$$\frac{\mathrm{d}\psi}{\mathrm{d}\xi} = 0, \qquad \frac{\mathrm{d}\psi^l}{\mathrm{d}\xi} = \Lambda\phi^s, \qquad \frac{\mathrm{d}\psi^s}{\mathrm{d}\xi} = -\Lambda(1-\phi^s). \qquad \text{(A2}a\text{–}c\text{)}$$

Solving the first of these equations implies that contours of constant

$$\psi = \psi_0, \qquad \text{(A3)}$$

https://doi.org/10.1017/jfm.2026.11311 Published online by Cambridge University Press

are the projected bulk particle paths. The isolines of the streamfunction, illustrated in figure 8, therefore correspond to the projection of the bulk particle paths into the $(\tilde{y}, \tilde{z})$ plane, as shown schematically in figure 12(*a*).

Gray & Ancey (2009) constructed a two-dimensional exact solution for the large-particle paths near a two-dimensional large-rich avalanche front, which shares many common features with the current problem. This paper therefore focusses on the paths of the small particles, and shows how this can be used to infer the paths of the large grains in Appendix B. A schematic diagram of a single small-particle path and how it relates to the structure of the breaking-size-segregation wave is shown in figure 12(*a*). Suppose that a particle path starts in the pure small region on the line $\tilde{z} = 1/2$, at (ξ_0, ψ_0), where

$$\psi_0 = \psi_m(\xi_0), \tag{A4}$$

and the function ψ_m is defined in (6.7). Within the pure region of small particles a small particle is simply swept along a particle-path $\psi = \psi_0$ unless it intersects with the line AB. It follows that for $\psi_0 \in [\psi_A, 0]$ the small particle enters the upper expansion fan at

$$\xi_1 = \xi_A + \frac{\psi_0 - \psi_A}{\Lambda}. \tag{A5}$$

Substituting the concentration in the upper fan (6.21) into (A2*c*) yields the ODE

$$\frac{\mathrm{d}(\psi - \psi_A)}{\mathrm{d}(\xi - \xi_A)} - \frac{\psi - \psi_A}{2(\xi - \xi_A)} = -\frac{\Lambda}{2}. \tag{A6}$$

This can be solved subject to the condition that the path enters at (ξ_1, ψ_0) to give

$$\psi = \psi_A - \Lambda(\xi - \xi_A) + 2\sqrt{\psi_0 - \psi_A}\sqrt{\Lambda(\xi - \xi_A)}, \tag{A7}$$

where the constant of integration has been simplified using (A5). The path travels through the top fan and intersects with the upper boundary of the eye (6.33) at

$$\xi_2 = \xi_A + \frac{\psi_0 - \psi_A}{(\phi^s_{eye})^2 \Lambda}, \qquad \psi_2 = \psi_A + \frac{(2\phi^s_{eye} - 1)(\psi_0 - \psi_A)}{(\phi^s_{eye})^2}, \tag{A8a,b}$$

where ϕ^s_{eye} is the constant concentration in the eye given by (6.32). Since the concentration in the eye is constant, it is easy to integrate the ODE (A2c) through the eye, subject to the initial condition that it starts at (ξ_2, ψ_2), to give the path through the upper eye

$$\psi = \psi_2 - \Lambda(1 - \phi^s_{eye})(\xi - \xi_2). \tag{A9}$$

This path reaches $\tilde{z} = 1/2$ at (ξ_3, ψ_3). The position that this occurs can be found by solving

$$\psi_3 = \psi_m(\xi_3) = \psi_2 - \Lambda(1 - \phi^s_{eye})(\xi_3 - \xi_2), \tag{A10}$$

iteratively for ξ_3. The path then moves into the lower domain where ϕ^s is still equal to the constant ϕ^s_{eye}. Solving (A2*c*) through the eye subject to the initial condition that the path starts at (ξ_3, ψ_3), implies that

$$\psi = \psi_3 - \Lambda(1 - \phi^s_{eye})(\xi - \xi_3). \tag{A11}$$

However, (A10) can be used to substitute for ψ_3 and show that the path through the lower eye is exactly equivalent to

$$\psi = \psi_2 - \Lambda(1 - \phi^s_{eye})(\xi - \xi_2), \tag{A12}$$

which is the same as the path through the upper eye (A9). Importantly, since the upper boundary of the eye (6.33) is the same as the lower boundary of the eye (6.36) and the

https://doi.org/10.1017/jfm.2026.11311 Published online by Cambridge University Press

path through the upper eye (A9) and the lower eye (A12) are the same, they must intersect at the same position. The lower intersection (ξ_4, ψ_4) is therefore the same as (ξ_2, ψ_2) in streamfunction coordinates, i.e.

$$\xi_4 = \xi_2, \qquad \psi_4 = \psi_2. \tag{A13a,b}$$

It should be noted that these are not the same physical points, as one is in the upper domain and the other in the lower, as shown on figure 12(*a*).

After crossing the lower boundary of the eye the path enters the lower expansion (6.27) and (A2*c*) implies that it satisfies the ODE

$$\frac{\mathrm{d}(\psi_C - \psi)}{\mathrm{d}(\xi_C - \xi)} - \frac{\psi_C - \psi}{2(\xi_C - \xi)} = -\frac{\Lambda}{2}. \tag{A14}$$

This can be solved to give the general solution

$$\psi_C - \psi = -\Lambda(\xi_C - \xi) + C\sqrt{\xi_C - \xi}, \tag{A15}$$

where C is a constant of integration. The path must pass through (ξ_2, ψ_2), which itself lies on the boundary of the lower eye (6.34). This fact can be used to show that

$$C = 2\phi^s_{eye}\Lambda\sqrt{\xi_C - \xi_2}. \tag{A16}$$

A more useful form for the constant C can be found by noting that the upper shock (6.25) intersects the upper boundary of the eye (6.33) at (ξ_C, ψ_C), which implies that

$$(\phi^s_{eye})^2\Lambda(\xi_C - \xi_A) = -\psi_A. \tag{A17}$$

In addition, adding and subtracting ξ_2 in the bracketed term on the left-hand side and substituting for $\xi_2 - \xi_A$ from (A8*a*) implies that

$$(\phi^s_{eye})^2\Lambda(\xi_C - \xi_2) = -\psi_0. \tag{A18}$$

Finally, combining (A15), (A16) and (A18) it follows that the path through the lower fan can be expressed as

$$\psi = \psi_C + \Lambda(\xi_C - \xi) - 2\sqrt{-\psi_0}\sqrt{\Lambda(\xi_C - \xi)}. \tag{A19}$$

From this form it is easy to show that the path through the lower fan (A19) intersects the lower shock (6.31) at

$$\xi_5 = \xi_C - \frac{1}{\Lambda}\left(\sqrt{-\psi_0} + \sqrt{-\psi_C}\right)^2, \qquad \psi_5 = \psi_0. \tag{A20a,b}$$

Since $\phi^s = 1$ in the pure small region the small-particle path equation (A2*c*) reduces to the bulk particle path equation (A2*a*) and it follows the bulk streamlines. Importantly, (A20) proves that the small-particle path exits the breaking wave on the ψ_0 streamline. It therefore rises up, passes across the $\tilde{z} = 1/2$ line for the second time at (ξ_0, ψ_0), reconnecting with the initially assumed path to form a closed loop, as shown in figure 12(*a*). The corresponding large-particle paths are constructed in a similar manner. In fact, equations (A2*b*,*c*) imply that the large-particle paths can be written down directly by using the mapping (6.37). For completeness the large-particle paths are summarised in Appendix B.

Appendix B. Large-particle paths in the projected plane

Using the mapping (6.37) it is possible to write down the expressions for the large-particle paths directly from the results for the small-particle paths in (A5), (A7), (A8), (A9), (A13),

https://doi.org/10.1017/jfm.2026.11311 Published online by Cambridge University Press

(A19) and (A20). The main difference is that the large particles are assumed to start on $\tilde{z} = 1/2$ in the pure large-particle region at (ξ_0, ψ_0), are drawn down to the base by the bulk flow and move upwards through the breaking-size-segregation wave instead of percolating downwards. A large particle in the pure large region follows a bulk projected particle path ψ_0 in the $(\tilde{y}, \tilde{z})$ plane unless $\psi_0 \in [\psi_C, 0]$ and it enters the lower expansion fan, intersecting the line CD at

$$\xi_1 = \xi_C - \frac{\psi_0 - \psi_C}{\Lambda}. \tag{B1}$$

The large particle then moves up through the lower expansion fan (6.27) along the path

$$\psi = \psi_C - \Lambda(\xi_C - \xi) + 2\sqrt{\psi_0 - \psi_C}\sqrt{\Lambda(\xi_C - \xi)}, \tag{B2}$$

until it intersects with the lower boundary of the eye (6.34) at

$$\xi_2 = \xi_C - \frac{\psi_0 - \psi_C}{(1 - \phi^s_{eye})^2 \Lambda}, \qquad \psi_2 = \psi_C - \frac{(2\phi^s_{eye} - 1)(\psi_0 - \psi_C)}{(1 - \phi^s_{eye})^2}. \tag{B3a,b}$$

The large particle then moves along the path

$$\psi = \psi_2 + \Lambda\phi^s_{eye}(\xi - \xi_2) \tag{B4}$$

and exits the eye at

$$\xi_4 = \xi_2, \qquad \psi_4 = \psi_2. \tag{B5a,b}$$

It then moves through the upper expansion fan (6.21) along the path

$$\psi = \psi_A + \Lambda(\xi - \xi_A) - 2\sqrt{-\psi_0}\sqrt{\Lambda(\xi - \xi_A)} \tag{B6}$$

and crosses the shock BC at

$$\xi_5 = \xi_A + \frac{1}{\Lambda}\left(\sqrt{-\psi_0} + \sqrt{-\psi_A}\right)^2, \qquad \psi_5 = \psi_0, \tag{B7a,b}$$

and in so doing reconnects with the ψ_0 bulk particle path to form a closed loop. In each vortex, the breaking-size-segregation wave facilitates the formation of two interpenetrating sub-vortices that rotate in the same direction as the bulk flow and recirculate the large and small particles, respectively, as shown in figure 12.

References

Baker, J., Johnson, C.G. & Gray, J.M.N.T. 2016*b* Segregation-induced finger formation in granular free-surface flows. *J. Fluid. Mech.* **809**, 168–212.

Barker, T. & Gray, J.M.N.T. 2017 Partial regularisation of the incompressible $\mu(I)$-rheology for granular flow. *J. Fluid. Mech.* **828**, 5–32.

Barker, T., Rauter, M., Maguire, E.S.F., Johnson, C.G. & Gray, J.M.N.T. 2021 Coupling rheology and segregation in granular flows. *J. Fluid Mech.* **909**, A22.

Barker, T., Schaeffer, D.G., Bohórquez, P. & Gray, J.M.N.T. 2015 Well-posed and ill-posed behaviour of the $\mu(I)$-rheology for granular flows. *J. Fluid. Mech.* **779**, 794–818.

Barker, T., Schaeffer, D.G., Shearer, M. & Gray, J.M.N.T. 2017 Well-posed continuum equations for granular flow with compressibility and $\mu(I)$-rheology. *Proc. R. Soc. A* **473**, 20160846.

Blasio, F.V.D. 2011 Landslides in Valles Marineris (Mars): a possible role of basal lubrication by sub-surface ice. *Planet. Space Sci.* **59**, 1384–1392.

Bodenschatz, E., Pesch, W. & Ahlers, G. 2000 Recent developments in Rayleigh-Bénard convection. *Annu. Rev. Fluid Mech.* **32**, 709–778.

Börzsönyi, T., Ecke, R.E. & McElwaine, J.N. 2009 Patterns in flowing sand: understanding the physics of granular flow. *Phys. Rev. Lett.* **103** (178302).

Brodu, N., Delannay, R., Valance, A. & Richard, P. 2015 New patterns in high-speed granular flows. *J. Fluid Mech.* **769**, 218–228.

https://doi.org/10.1017/jfm.2026.11311 Published online by Cambridge University Press

BRODU, N., RICHARD, P. & DELANNAY, R. 2013 Shallow granular flows down flat frictional channels: steady flows and longitudinal vortices. *Phys. Rev. E* **87**, 022202.
CAMPBELL, C.S. 1989 Self-lubrication for long runout landslides. *J. Geol.* **97** (6), 653–665.
CHADWICK, P. 1976 *Continuum Mechanics. Concise Theory and Problems*. George Allen & Unwin.
COLLINS, G.S. & MELOSH, H.J. 2003 Acoustic fluidization and the extraordinary mobility of sturzstroms. *J. Geophys. Res.* **108** (B10), 2473.
DADE, W.B. & HUPPERT, H.E. 1998 Long-runout rockfalls. *Geology* **26**, 803–806.
D'ORTONA, U., MARTINAND, D. & THOMAS, N. 2025 Rayleigh–Taylor instability in two-layer granular flows. *Phys. Rev. E* **112**, 015421.
D'ORTONA, U. & THOMAS, N. 2020 Self-induced Rayleigh–Taylor instability in segregating dry granular flows. *Phys. Rev. Lett.* **124**, 178001.
DSOUZA, P.V. & NOTT, P.R. 2020 A non-local constitutive model for slow granular flow that incorporates dilatancy. *J. Fluid Mech.* **888**, R3.
DSOUZA, P.V. & NOTT, P.R. 2021 Dilatancy-driven secondary flows in dense granular materials. *J. Fluid Mech.* **914**, A36.
DUFRESNE, A. & DAVIES, T.R. 2009 Longitudinal ridges in mass movement deposit. *Geomorphology* **105**, 171–181.
EDWARDS, A.N. & GRAY, J.M.N.T. 2015 Erosion-deposition waves in shallow granular free-surface flows. *J. Fluid Mech.* **762**, 35–67.
EDWARDS, A.N., ROCHA, F.M., KOKELAAR, B.P., JOHNSON, C.G. & GRAY, J.M.N.T. 2023 Particle-size segregation in self-channelised granular flows. *J. Fluid Mech.* **995**, A38.
ESHUIS, P., VAN DER WEELE, K., VAN DER MEER, D. & LOHSE, D. 2005 Granular Leidenfrost effect: experiment and theory of floating particle clusters. *Phys. Rev. Lett.* **95**, 258001.
FORTERRE, Y. & POULIQUEN, O. 2001 Longitudinal vortices in granular flows. *Phys. Rev. Lett.* **86**, 5886.
FORTERRE, Y. & POULIQUEN, O. 2002 Stability analysis of rapid granular flows: formation of longitudinal vortices. *J. Fluid Mech.* **46**, 361–387.
GADAL, C., JOHNSON, C.G. & GRAY, J.M.N.T. 2026 Surface curvature and secondary vortices in steady dense shallow granular flows. *J. Fluid Mech.* **1027**, A34.
GDR-MiDi 2004 On dense granular flows. *Eur. Phys. J. E* **14**, 341–365.
GODDARD, J.D. & LEE, J. 2018 Regularization by compressibility of the $\mu(I)$ model of dense granular flow. *Phys. Fluids* **30**, 073302.
GOLDHIRSCH, I. 2003 Rapid granular flows. *Annu. Rev. Fluid Mech.* **35**, 267–293.
GRAY, J.M.N.T. 2001 Granular flow in partially filled slowly rotating drums. *J. Fluid Mech.* **441**, 1–29.
GRAY, J.M.N.T. 2018 Particle segregation in dense granular flows. *Annu. Rev. Fluid Mech.* **50**, 407–433.
GRAY, J.M.N.T. & ANCEY, C. 2009 Segregation, recirculation and deposition of coarse particles near two-dimensional avalanche fronts. *J. Fluid Mech.* **629**, 387–423.
GRAY, J.M.N.T. & ANCEY, C. 2011 Multi-component particle size-segregation in shallow granular avalanches. *J. Fluid Mech.* **678**, 535–588.
GRAY, J.M.N.T. & ANCEY, C. 2015 Particle-size and particle-density segregation in granular avalanches. *J. Fluid Mech.* **779**, 622–668.
GRAY, J.M.N.T. & EDWARDS, A.N. 2014 A depth-averaged $\mu(I)$-rheology for shallow granular free-surface flows. *J. Fluid Mech.* **755**, 503–544.
GRAY, J.M.N.T. & KOKELAAR, B.P. 2010*a* Erratum large particle segregation, transport *a*nd accumulation in granular free-surface flows – erratum. *J. Fluid Mech.* **657**, 539.
GRAY, J.M.N.T. & KOKELAAR, B.P. 2010*b* Large particle segregation, transport and accumulation in granular free-surface flows. *J. Fluid Mech.* **652**, 105–137.
GRAY, J.M.N.T. & THORNTON, A.R. 2005 A theory for particle size segregation in shallow granular free-surface flows. *Proc. R. Soc. A* **461**, 1447–1473.
HEYMAN, J., BOLTENHAGEN, P., DELANNAY, R. & VALANCE, A. 2017*a* Experimental investigation of high speed granular flows down inclines. *EPJ Web Conf.* **140**, 03057.
HEYMAN, J., DELANNAY, R., TABUTEAU, H. & VALANCE, A. 2017*b* Compressibility regularizes the $\mu(I)$-rheology for dense granular flows. *J. Fluid Mech.* **830**, 553–568.
JENKINS, J.T. & SAVAGE, S.B. 1983 A theory for the rapid flow of identical, smooth, nearly elastic, spherical particles. *J. Fluid Mech.* **130**, 187–202.
JOHNSON, C.G., KOKELAAR, B.P., IVERSON, R.M., LOGAN, M., LAHUSEN, R.G. & GRAY, J.M.N.T. 2012 Grain-size segregation and levee formation in geophysical mass flows. *J. Geophys. Res.* **117**, F01032.
JOP, P., FORTERRE, Y. & POULIQUEN, O. 2005 Crucial role of sidewalls in granular surface flows: consequences for the rheology. *J. Fluid Mech.* **541**, 167–192.

https://doi.org/10.1017/jfm.2026.11311 Published online by Cambridge University Press

JOP, P., FORTERRE, Y. & POULIQUEN, O. 2006 A constitutive relation for dense granular flows. *Nature* **44**, 727–730.
KIM, S. & KAMRIN, K. 2023 A second-order non-local model for granular flows. *Front. Phys.* **11**, 1092233.
KRISHNARAJ, K.P. & NOTT, P.R. 2016 A dilation-driven vortex flow in sheared granular materials explains a rheometric anomaly. *Nat. Commun.* **7**, 10630.
KURGANOV, A. & TADMOR, E. 2000 New high-resolution central schemes for nonlinear conservationl laws and convection-diffusion equations. *J. Comput. Phys.* **160**, 241–282.
MAGARINI, G., MITCHELL, T.M., GRINDROD, P.M., SCHMITT, H.H. & PETRO, N.E. 2021 Scaling relationship between the wavelength of longitudinal ridges and the thickness of long runout landslides on the Moon. *J. Geophys. Res.: Planets* **126**, e2021JE006922.
MAGNARINI, G., CHAMPAGNE, A., MORINO, C., BECK, C., PHILIPPE, M., DECAULNE, A. & CONWAY, S.J. 2024 Long-runout landslides with associated longitudinal ridges in Iceland as analogues of Martian landslide deposits. *Earth Surf. Dyn.* **12**, 657–678.
MAGNARINI, G., MITCHELL, T.M., GRINDROD, P.M., GOREN, L. & SCHMITT, H.H. 2019 Longitudinal ridges imparted by high-speed granular flow mechanisms in Martian landslides. *Nat. Commun.* **10**, 4711.
MAGUIRE, E.S.F., BARKER, T., RAUTER, M., JOHNSON, C.G. & GRAY, J.M.N.T. 2024 Particle-size segregation patterns in a partially filled triangular rotating drum. *J. Fluid Mech.* **979**, A40.
MCELWAINE, J.N., TAKAGI, D. & HUPPERT, H.E. 2012 Surface curvature of steady granular flows. *Granul. Matter* **14**, 229–234.
MCSAVENEY, M.J. 1978 Sherman glacier rock avalanche, Alaska, U.S.A. In *Rockslides and Avalanches, 1: Natural Phenomena*, chap. 6. In *Developments in Geotechnical Engineering* (ed. B. Voight), vol. 14, pp. 97–258. Elsevier.
MELOSH, H.J. 1979 Acoustic fluidization: a new geologic process? *J. Geophys. Res.* **84** (B13), 7513–7520.
NEVEU, A., LARCHER, M., DELANNAY, R., JENKINS, J.T. & VALANCE, A. 2022 Particle segregation in inclined high-speed granular flows. *J. Fluid Mech.* **935**, A41.
PEARSE, A., JOHNSON, C.G. & GRAY, J.M.N.T. Transversely-segregated longitudinal stripes in bidisperse granular flows. *J. Fluid Mech.*
POST, A. 1967 Effects of the March 1964 Alaska earthquake on glaciers. *U.S. Geol. Surv. Prof. Paper* **544-D**, 42,
POULIQUEN, O., DELOUR, J. & SAVAGE, S.B. 1997 Fingering in granular flows. *Nature* **386**, 816–817.
ROCHA, F.M., JOHNSON, C.G. & GRAY, J.M.N.T. 2019 Self-channelization and levee formation in monodisperse granular flows. *J. Fluid Mech.* **876**, 591–641.
SAVAGE, S.B. & LUN, C.K.K. 1988 Particle size segregation in inclined chute flow of dry cohesionless granular solids. *J. Fluid Mech.* **189**, 311–335.
SCHAEFFER, D.G., BARKER, T., TSUJI, D., GREMAUD, P., SHEARER, M. & GRAY, J.M.N.T. 2019 Constitutive relations for compressible granular flow in the inertial regime. *J. Fluid Mech.* **874**, 926–951.
SHREVE, R.L. 1966 Sherman landslide, Alaska. *Science* **154** (3757), 1639–1643.
SILBERT, L.E., LANDRY, J.W. & GREST, G.S. 2003 Granular flow down a rough inclined plane: transition between thin and thick piles. *Phys. Fluids* **15**, 1–10.
SRIVASTAVA, I., SILBERT, L.E., GREST, G.S. & LECHMAN, J.B. 2021 Viscometric flow of dense granular materials under controlled pressure and shear stress. *J. Fluid Mech.* **907**, A18.
THORNTON, A.R. & GRAY, J.M.N.T. 2008 Breaking size-segregation waves and particle recirculation in granular avalanches. *J. Fluid Mech.* **596**, 261–284.
THORNTON, A.R., GRAY, J.M.N.T. & HOGG, A.J. 2006 A three-phase mixture theory for particle size segregation in shallow granular free-surface flows. *J. Fluid Mech.* **550**, 1–25.
TREWHELA, T., ANCEY, C. & GRAY, J.M.N.T. 2021 An experimental scaling law for particle-size segregation in dense granular flows. *J. Fluid Mech.* **916**, A55.
TRUESDELL, C.A. 1977 *A First Course in Rational Continuum Mechanics*. Academic Press.
TRUESDELL, C. & NOLL, W. 2004 *The Non-Linear Field Theories of Mechanics*. Springer.
VIROULET, S., BAKER, J.L., ROCHA, F.M., JOHNSON, C.G. & GRAY, J.M.N.T. 2018 The kinematics of bidisperse granular roll waves. *J. Fluid Mech.* **848**, 836–875.
WOODHOUSE, M.J., THORNTON, A.R., JOHNSON, C.G., KOKELAAR, B.P. & GRAY, J.M.N.T. 2012 Segregation-induced fingering instabilities in granular free-surface flows. *J. Fluid Mech.* **709**, 543–580.

https://doi.org/10.1017/jfm.2026.11311 Published online by Cambridge University Press